Originally published as:

Modification of the Seismic Properties of Subducting Continental Crust by Eclogitization and Deformation Processes

Sascha Zertani[1] , Timm John[1], Frederik Tilmann[1,2] , Hem B. Motra[3] , Ruth Keppler[4] , Torgeir B. Andersen[5] , and Loic Labrousse[6]

[1]Institute of Geological Sciences, Freie Universität Berlin, Berlin, Germany, [2]Deutsches GeoForschungsZentrum, Potsdam, Germany, [3]Department of Geosciences, Marine and Land Geomechanics and Geotechnics, University of Kiel, Kiel, Germany, [4]Institute of Geosciences and Meteorology, University of Bonn, Bonn, Germany, [5]The Centre of Earth Evolution and Dynamics (CEED), Department of Geosciences, University of Oslo, Oslo, Norway, [6]Sorbonne Université, CNRS-INSU, Institut des Sciences de la Terre Paris, ISTeP, UMR 7193, Paris, France

Abstract Subduction zone processes and the resulting geometries at depth are widely studied by large-scale geophysical imaging techniques. The subsequent interpretations are dependent on information from surface exposures of fossil subduction and collision zones, which help to discern probable lithologies and their structural relationships at depth. For this purpose, we collected samples from Holsnøy in the Bergen Arcs of western Norway, which constitutes a well-preserved slice of continental crust, deeply buried and partially eclogitized during Caledonian collision. We derived seismic properties of both the lower crustal granulite-facies protolith and the eclogite-facies shear zones by performing laboratory measurements on cube-shaped samples. P and S wave velocities were measured in three perpendicular directions, along the principal fabric directions of the rock. Resulting velocities agree with seismic velocities calculated using thermodynamic modeling and confirm that eclogitization causes a significant increase of the seismic velocity. Further, eclogitization results in decreased V_P/V_S ratios and, when associated with deformation, an increase of the seismic anisotropy due to the crystallographic preferred orientation of omphacite that were obtained from neutron diffraction measurements. The structural framework of this exposed complex combined with the characteristic variations of seismic properties from the lower crustal protolith to the high-pressure assemblage provides the possibility to detect comparable structures at depth in currently active settings using seismological methods such as the receiver function method.

1. Introduction

Large-scale geophysical imaging techniques are widely used to study subduction and collision zones to discern geometries and processes active at depth (e.g., Bostock et al., 2002; Halpaap et al., 2018; Rondenay et al., 2008; Schiffer et al., 2015). Particularly, the receiver function method (e.g., Kind et al., 2012), which utilizes the conversion of P to S waves and vice versa at boundaries with contrasting impedance, is ideal to image the structure of subducted crust, as it highlights interfaces associated with contrasting seismic properties. Typically, the descending crust is well imaged in the shallow section of subduction/collision zones and often disappears from the geophysical record in its deeper regions (e.g., Rondenay et al., 2001; Schneider et al., 2013). This is usually attributed to the transformation of crustal rocks into eclogites, essentially removing the velocity contrast to the surrounding mantle (Hacker et al., 2003; Hetényi et al., 2007; Rondenay et al., 2008). However, the crustal signal does not disappear abruptly, but a transitional zone, characterized by progressive blurring of the signal, is typically observed (e.g., Halpaap et al., 2018; Schneider et al., 2013). This is presumably caused by partial eclogitization of the downgoing crust, a process seemingly active at depth beneath the Himalaya-Tibet collision system today, where the signal of the Indian lower crust decreases progressively while its density increases (Hetényi et al., 2007; Nabelek et al., 2009). Additionally, intense shear in subduction or collision settings can produce seismically anisotropic fabrics due to the alignment of anisotropic minerals (Faccenda et al., 2019; Lloyd, Halliday, et al., 2011). Such anisotropic structures can, for example, be identified in receiver function images by contrasting images from different backazimuthal ranges (Schulte-Pelkum et al., 2005).

To quantitatively assess the imprint of ongoing eclogitization on seismic images, it is important to combine knowledge of how eclogitization alters the seismic properties of the rocks with the geodynamic and structural framework of subduction and collision zones at various scales. It has been shown that dry crustal rocks can remain metastable throughout significant ranges of changing *P-T* conditions without any signs of ductile deformation or reequilibration of the mineral assemblage (Austrheim, 1987; Jackson et al., 2004; Scambelluri et al., 2017). While some studies suggest that ductile deformation of dry metastable crustal rocks can be facilitated by extreme grain size reduction (Hawemann et al., 2019; Menegon et al., 2017), the introduction of external fluids is acknowledged as the most effective trigger for ductile deformation and eclogitization (e.g., Austrheim, 1987; John & Schenk, 2003). After fluid infiltration, eclogitization dominantly progresses with two closely linked mechanisms: (1) mainly associated with deformation (dynamic eclogitization) and (2) controlled by fluid-mediated dissolution, transport, and precipitation processes (static eclogitization; e.g., Austrheim, 1987; John & Schenk, 2003; Zertani et al., 2019). Both mechanisms can be active simultaneously with areas of the rock volume being dominated by one or the other, leading to varying associations between strain and eclogitization on the outcrop or even regional scale (e.g., Zertani et al., 2019), which in turn affects the expected seismic signal in geophysical studies.

While bulk *P* and *S* wave velocities are mainly controlled by the mineral assemblage (Hacker et al., 2003), characteristics such as lithological layering, shape preferred orientations (SPOs), and crystallographic preferred orientations (CPOs) produce seismic anisotropy and further modify *P* and S wave velocities (e.g., Bascou et al., 2001; Faccenda et al., 2019; Keppler et al., 2017; Zhong et al., 2014). Two alternative approaches to determine the seismic properties of rocks are laboratory measurements (e.g., Almqvist et al., 2013; Kern, 1978) and calculations based on modal mineral proportions (e.g., Almqvist et al., 2013; Hacker et al., 2003). Previous studies typically reported *P* wave velocities of up to 8.4 km/s or even higher for eclogites, depending on the mineral assemblage, and *S* wave velocities between 4.2 and 4.8 km/s (e.g., Ábalos et al., 2011; Babuška et al., 1978; Fountain et al., 1994; Manghnani et al., 1974, Wang et al., 2005a, 2005b). The directional dependence of seismic velocities has been of particular interest; *P* wave anisotropy for eclogites was generally found to be below ~6% (e.g., Fountain et al., 1994; Wang et al., 2005a) and was usually attributed to the CPO of omphacite (e.g., Bascou et al., 2001). Granulites, representative for the lower continental crust, typically have *P* wave velocities of 6.5–7.5 km/s and *S* wave velocities of 3.5–4.2 km/s (e.g., Barruol & Kern, 1996; Brown et al., 2009; Manghnani et al., 1974; Weiss et al., 1999). *P* wave anisotropy in granulites varies strongly from <1% up to >7%, depending on the mineral assemblage (e.g., Brown et al., 2009).

Nevertheless, measurements and calculations of the petrophysical properties are usually limited to the scale of hand specimens, which is far below the wavelengths typically used in large-scale geophysical imaging (e.g., Rondenay et al., 2005). It is therefore necessary to not only investigate the sample properties but to combine the results with the large-scale structures associated with the formation of the rocks to upscale the measured properties.

In this study we investigate the effect of eclogite-facies metamorphism and deformation during continental collision on the seismic properties of lower continental crust. Therefore, we measured *P* and *S* wave velocities, their anisotropy, and pressure and temperature dependence in the laboratory and compare the results with seismic velocities calculated from thermodynamic modeling. Additionally, the resulting seismic anisotropy is compared to CPOs obtained from neutron diffraction measurements. For this we sampled anorthositic granulites and eclogites from a fossil collision zone exposed on Holsnøy in the Bergen Arcs, western Norway. Seismic velocity measurements were also performed on an eclogite strongly retrogressed in the amphibolite facies to constrain the effect of retrogression. We combine the results with our knowledge of the structural setting and show that eclogitization and deformation significantly modify the petrophysical properties of the lower crustal rocks. Since the structures on Holsnøy are acknowledged to be representative of the structures found at depth in currently active collision settings, we discuss some of their characteristic signatures in seismic imaging methods.

2. Geological Setting

2.1. Geodynamic Context

The Scandinavian Caledonides are the result of the Scandian collision of Baltica and Laurentia between 430 and 400 Ma (Corfu et al., 2014). After closure of the Iapetus Ocean, the leading edge of the hyperextended

pre-Caledonian margin of Baltica constituted the lower plate during incipient continental collision (Andersen et al., 1991, 2012). Part of this hyperextended margin, the Jotun-Lindås-Dalsfjord microcontinent or continental sliver, is now exposed as the Jotun, Lindås, and Dalsfjord nappe complexes in Norway (Jakob et al., 2017, 2019).

The Lindås nappe, which is part of the Bergen Arcs (western Norway), is composed of magmatic rocks of the anorthosite, mangerite, charnockite, and granite AMCG (anorthosite, mangerite, charnockite, and granite) suite, which have been equilibrated at granulite-facies conditions (~1 GPa and 800 °C) at ~930 Ma (Austrheim & Griffin, 1985; Bingen et al., 2001). In the following ~500 Myrs, the *P-T* conditions at which these rocks resided are unclear. They, however, show no signs of significant alteration between Precambrian times and the Caledonian collision, suggesting that no significant exhumation took place and that they likely cooled to temperatures reflecting an average stable shield geotherm, representative of lower continental crust (Jamtveit et al., 1990).

During the Caledonian collision the rocks of the Lindås nappe were exposed to eclogite-facies conditions (peak at ~430 Ma; Glodny et al., 2008), when the hyperextended pre-Caledonian margin was incorporated into the collision zone with peak *P-T* conditions of ~2 GPa and ~700 °C (e.g., Altenberger & Wilhelm, 2000; Bhowany et al., 2017; Jamtveit et al., 1990). However, the Lindås nappe did not reequilibrate in its entirety (Figure 1), preserving large volumes of granulite throughout eclogite-facies metamorphism and exhumation (Austrheim, 1987, 1990). The exhumed lower crustal complex on Holsnøy therefore experienced *P-T* conditions similar to those expected from the Indian lower crust underplating the Asian crust beneath southern Tibet at present day (Labrousse et al., 2010) and constitutes one of the best exposed analogues of the prograde behavior of lower continental crust buried to eclogite-facies conditions.

2.2. Structural Relationships on Holsnøy

The main eclogite-facies exposures of the Lindås nappe are found on the island of Holsnøy (Austrheim, 1987; Figure 1), located approximately 20 km north of Bergen. Here eclogite-facies shear zones of variable scale crosscut granulite-facies rocks of the AMCG suite (Austrheim, 1987; Austrheim & Griffin, 1985; Boundy et al., 1992). Additionally, a significant portion of the rock volume has reequilibrated without associated deformation (Zertani et al., 2019). Eclogite-facies metamorphism is closely linked to brittle fracturing and subsequent fluid infiltration, leaving large volumes of the granulite unaltered when there is no fluid present (Austrheim, 1987; Incel et al., 2019; Raimbourg et al., 2005). Brittle fracturing of the rock at eclogite-facies *P-T* conditions is clearly documented by the occurrence of eclogite-facies pseudotachylytes (Austrheim et al., 2017; Austrheim & Boundy, 1994; Petley-Ragan et al., 2018), and associated fractures provide ideal pathways for fluid infiltration (e.g., Jamtveit et al., 2018).

With progressive ductile deformation during fluid infiltration small-scale shear zones evolve to form shear zone networks (Austrheim, 1987; Jolivet et al., 2005; Raimbourg et al., 2005), which combine into larger-scale shear zones, up to a few hundred meters wide (Boundy et al., 1992; Zertani et al., 2019; see Figure 1). Additionally, they are typically surrounded by the so-called sheared eclogite breccia, which has a sheared eclogite matrix surrounding preserved granulite blocks (Boundy et al., 1992; Zertani et al., 2019). It thus constitutes a petrological and structural transition from the unaltered and undeformed granulitic protolith to highly eclogitized and highly strained domains. These transition zones are often thicker than the main shear zone itself (Zertani et al., 2019).

3. Methods

3.1. Laboratory Measurements

P and *S* wave velocity measurements were performed at the University of Kiel (Germany) in a true triaxial multianvil press using the ultrasonic pulse transmission technique (Kern, 1978; Kern & Fakhimi, 1975) on rock cubes with a 43 mm edge length. The sample cubes were prepared with their edges parallel to the three (macroscopically visible) principal fabric directions of the rock; i.e., *x* within the foliation plane and parallel to the lineation, *y* within the foliation plane and perpendicular to the lineation, and *z* perpendicular to the foliation. A complete set of measurements includes three *P* wave velocities (*x*, *y*, and *z* directions) and six *S* wave velocities (two perpendicular polarization directions for each of the three axis). *P* and *S* wave velocities were obtained using transducers operating at 2 MHz for *P* waves and 1 MHz for *S* waves. Near-hydrostatic
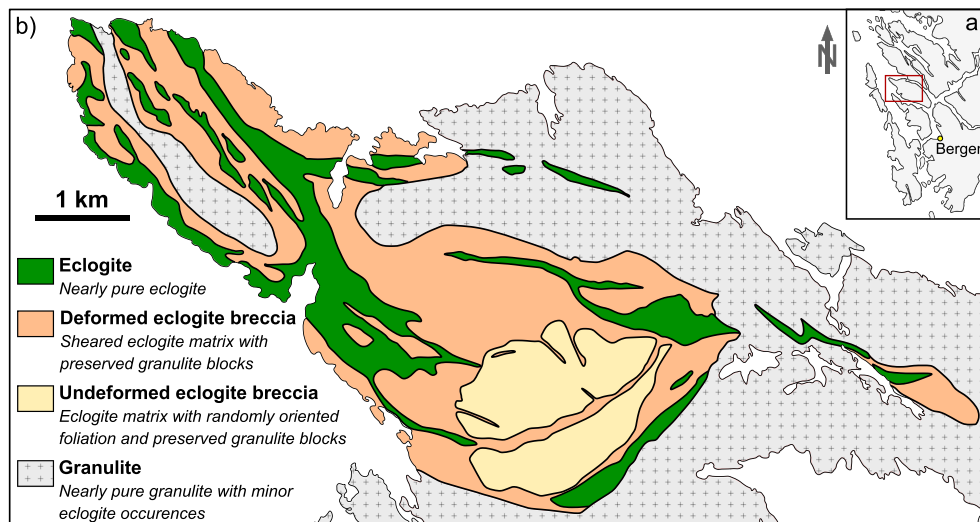
Figure 1. Geological map of northwestern Holsnøy showing the distribution of eclogite exposures. The inset (a) shows the location of the map in western Norway near the city of Bergen. The map (b) was compiled and modified from Jolivet et al. (2005) and Zertani et al. (2019).

conditions were achieved with six pyramidal pistons. The respective velocities were calculated from the distance traveled by the wave, which is obtained from the piston displacement, and the time needed for a wave to travel through the sample. Measurements were performed in three cycles: (1) During the pressure cycle the applied pressure was increased stepwise (50 MPa steps) from ambient conditions up to 600 MPa and then released with the same step size. (2) During the second cycle both pressure and temperature were increased at the same time, from ambient conditions (20 °C and 0 MPa) up to 600 °C and 600 MPa in steps of 100 MPa and 100 °C, respectively. (3) During the release path temperature was reduced in 100 °C steps until reaching ambient temperature conditions, while pressure was held at 600 MPa. Only after the temperature returned to ambient conditions pressure was released in steps of 50 MPa. After each heating step, the sample was given 30 min to ensure an equilibrated temperature throughout the sample and velocities were measured after each pressure and temperature change. This measurement setup ensures that changes in P and S wave velocities with pressure and temperature can be quantified independently. For a detailed description of the instrumental setup see Kern et al. (1997) and Motra and Zertani (2018).

3.2. Thermodynamic Modeling

Thermodynamic modeling was performed using the PerpleX software package (Connolly, 2005; Connolly & Kerrick, 2002), which minimizes the Gibbs energy to compute the most stable mineral assemblage at given P-T conditions. P and S wave velocities are then computed as Voigt-Reuss-Hill averages (Hill, 1952). In this study we calculate P and S wave velocities for both eclogites and granulites at eclogite-facies conditions. To do so, the internally consistent thermodynamic database of Holland and Powell (1998, updated in 2002) was used, because it includes shear moduli, necessary for seismic velocity calculations. The calculations were done in the Mn-Na-Ca-K-Fe-Mg-Al-Si-Ti-H_2O system using the following solution phase models: pyroxene and mica (Holland & Powell, 1996), garnet (White et al., 2005), feldspar (Furman & Lindsley, 1988), amphibole (Diener et al., 2007), and epidote (Holland & Powell, 1998). For eclogites, we implemented the solution model for omphacitic pyroxenes from Green et al. (2007).

The calculations were performed based on X-ray fluorescence (XRF) whole-rock analysis of 14 eclogites and eight granulites (Table **S6** in the supporting information). XRF analysis was performed on sample powders, which were dried prior to analysis (at 105 °C) and then measured using a Panalytical Axios Advanced at the German Research Center for Geosciences (GFZ, Potsdam). P and S wave velocities were calculated for conditions of 2 GPa and 700 °C, which reflect reasonable peak P-T estimates for the eclogite assemblages exposed on Holsnøy (Bhowany et al., 2017; Jamtveit et al., 1990). In order to obtain P and S wave velocities for granulites, calculations were done for conditions representative of the granulite-facies peak (1 GPa and 800 °C; Austrheim & Griffin, 1985). Then P and S wave velocities were extrapolated up to eclogite-facies

conditions using the pressure and temperature derivatives that are returned by the thermodynamic calculations. This step is necessary to retrieve seismic properties of a metastable paragenesis.

Calculations for granulites were performed without H_2O, assuming that the minor hydrous phases present in thin section (e.g., zoisite needles included in plagioclase) are a result of later rehydration and do not represent the original granulite-facies mineral assemblage (e.g., Austrheim & Griffin, 1985). Eclogite paragenesis, however, were calculated with H_2O in excess, because they form during continuous fluid infiltration (Austrheim, 1987), suggesting that availability of fluids is larger than the fluid consumption during eclogitization. The Fe contents were assumed to be purely Fe^{2+}, since the only Fe^{3+}-bearing phase in thin section is clinozoisite (X_{Ep} <0.15) and the amount of Fe^{3+} in the bulk sample is therefore negligible.

3.3. Neutron Diffraction

In order to link the directional dependence of the seismic properties with CPOs, selected samples were analyzed using the time-of-flight (TOF) neutron texture diffractometer SKAT at the Frank Laboratory of Neutron Physics at the Joint Institute of Nuclear Research in Dubna, Russia (Keppler et al., 2014; Ullemeyer et al., 1998). In contrast to other methods, such as electron backscatter diffraction (EBSD), TOF neutron diffraction provides the opportunity to analyze large sample volumes, which is specifically important when measuring coarse-grained samples. Measurements were performed on roughly isometric samples with a maximum diameter of 5 cm, which were rotated in 10° steps every 2,200 s. In order to cover the entire area of the pole figure, 19 detectors are aligned on a ring at 90° from the sample, yielding a constant Bragg angle. For detailed descriptions of the instrument setup see Keppler et al. (2014). The obtained spectra were analyzed using the MAUD software (Lutterotti et al., 1997).

4. Sample Description

We measured seismic velocities of three granulites, three eclogites, and one retrogressed eclogite. Granulites and eclogites were chosen to reflect the variability of the rocks exposed on Holsnøy that show no signs of significant retrogression. Of the selected samples, two eclogites and two granulites were further analyzed with neutron diffraction. Finally, 22 samples were selected for thermodynamic modeling. Sample locations are shown in the supporting information (Figure S1). Bulk rock compositions, which were acquired using XRF analysis (Table S6), and representative electron microprobe analysis of the main mineral phases (Tables S1 and S2) are summarized in the supporting information. Modal abundances of the main minerals given in this section were approximated using scanning electron microscopy mapping on thin sections (Tables S3 and S4) with a Zeiss Sigma 300 field emission scanning electron microscope equipped with an EDS system consisting of two Bruker XFlash 6, 60 mm^2 silicon drift detectors. Operating conditions were 20 kV with an aperture size of 60 μm and 0.02 s dwell time for each pixel analysis.
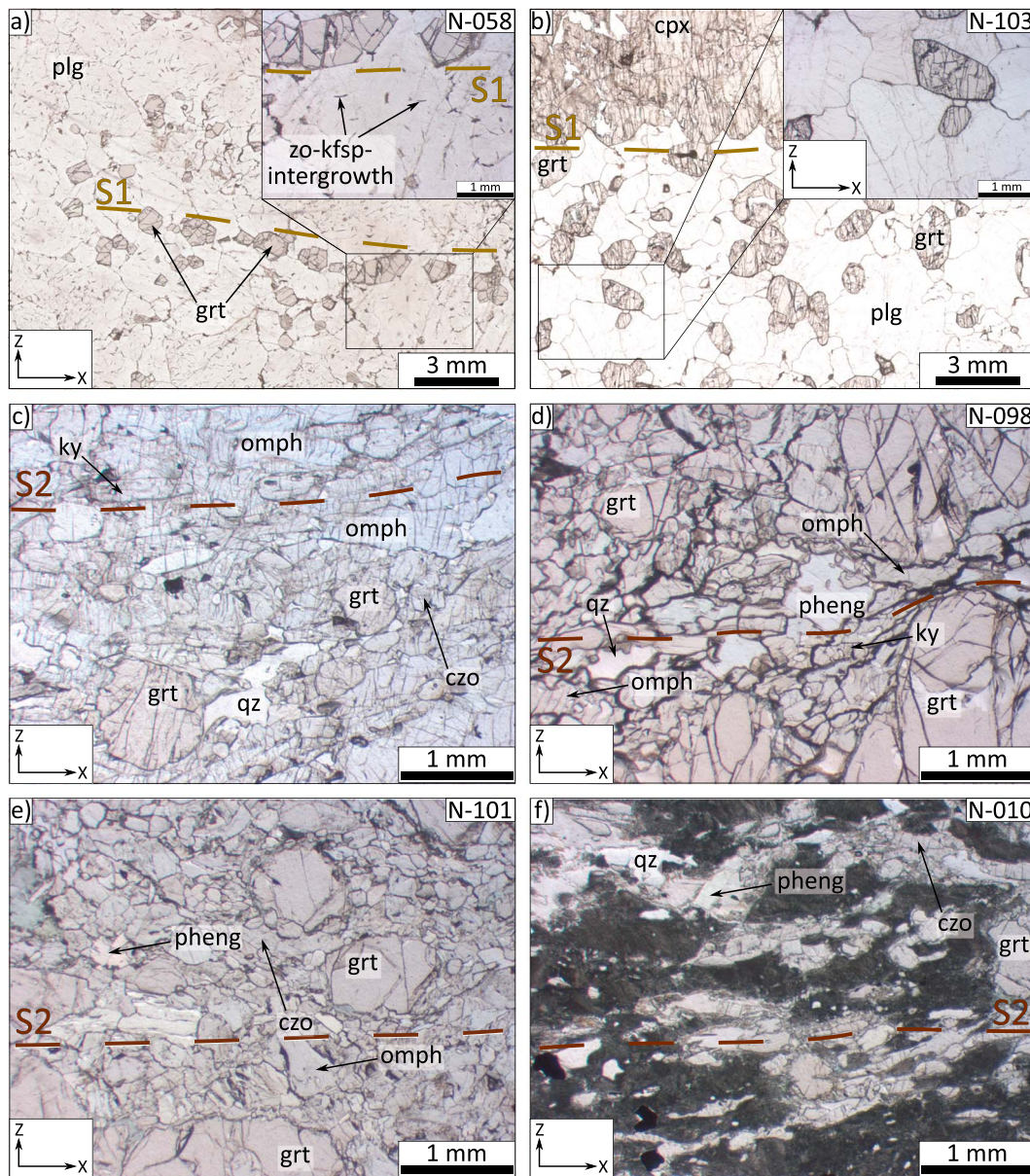
4.1. Samples for Laboratory Measurements and Neutron Diffraction
4.1.1. Granulite (Samples N-058 and N-103)
Sample N-058 is composed of >90 vol% plagioclase, ~5 vol% garnet, ~5 vol% clinopyroxene, and accessory scapolite. For velocity laboratory measurements, two sample cubes of the sample were prepared to account for the heterogeneous distribution of garnet and pyroxene. In N-058B, pyroxene (~15 vol%) and garnet (~10 vol%) are more abundant, compared to N-058A (<5 vol% and ~5 vol%, respectively). Sample N-103 is also mainly composed of plagioclase (~50 vol%); however, clinopyroxenes (~15 vol%) and garnet (~35 vol%) are significantly more abundant than in N-058.

Both samples have a coarse-grained (up to 1 cm) plagioclase matrix (Figures 2a and 2b) and coronas composed of clinopyroxene in the central part surrounded by garnet. These coronas are often flattened and form the foliation (Figure 2b), which is thus dominated by a compositional banding rather than the SPO of individual grains. The coronas are also slightly elongated, forming a weak stretching lineation. Further, garnet grains within the plagioclase matrix are often aligned parallel to the flattened coronas, thus forming garnet strings that also contribute to strengthen the foliation (Figure 2a).

Sample N-103 has clinopyroxene and garnet grains with grain sizes of ~7–8 mm, whereas garnets and clinopyroxenes in N-058 are ~3 mm in size. Both samples show almost no signs of alteration, except for up to 5-μm-sized zoisite needles typically intergrown with K-feldspar along plagioclase grain boundaries (Figure 2a). Plagioclase grains are isometric in both samples. Garnet-clinopyroxene coronas are most

Figure 2. Photographs of thin sections from the samples used for laboratory velocity measurements and neutron diffraction measurements showing the main mineral phases and representative microstructures. In each image, *x* (parallel to the lineation) is horizontal and *z* (perpendicular to the foliation) is vertical. Further, the trend of the foliation (S1 or S2) is shown as a dashed line. (a) Sample N-058, of which two aliquots were used for laboratory measurements. The compositional banding (macroscopic foliation) is mainly produced by aligned garnet that are parallel to elongate aggregates of garnet and clinopyroxene. The inset shows the same thin section at higher magnification. (b) Sample N-103, which compared to N-058 has less aggregates of zoisite/K-feldspar (hydration product). The inset shows the same thin section at higher magnification. (c) Sample N-059 is a fresh eclogite. The foliation is formed by the shape preferred orientation (SPO) of omphacite, kyanite, and clinozoisite. (d) Sample N-098 has a similar mineral assemblage as N-059; however, garnet grains are significantly larger. (e) N-101 exhibits a less pronounced SPO of omphacite than N-059. (f) N-010 is strongly retrogressed and preserves the eclogite-facies mineral assemblage only in patches. Abbreviations: grt = garnet; zo = zoisite; kfsp = K-feldspar; plg = plagioclase; omph = omphacite; ky = kyanite; qz = quartz; czo = clinozoisite; pheng = phengite.

abundant in N-103 among our samples, followed by N-058A and then N-058B. Since they are the main feature forming the granulite-facies foliation (S1), the foliation is most pronounced in N-103 and least pronounced in N-058A, where the foliation is mostly produced by the linear alignment of garnet.

4.1.2. Eclogite (Samples N-059, N-098, and N-101)

The main constituting minerals in N-059 are ~55 vol% omphacite, ~15 vol% kyanite, ~10 vol% garnet, ~10 vol% quartz, and <10 vol% clinozoisite. N-098 contains ~60 vol% omphacite, ~25 vol% garnet, ~10 vol%

phengite, and minor kyanite and quartz (<5 vol% in total). N-101 consists of ~50 vol% omphacite, 40 vol% garnet, ~10 vol% kyanite, and accessory phengite, quartz, and clinozoisite.

The eclogites are fine grained with grain sizes generally well below 1 mm (Figures 2c–2e) with only garnet grains being larger (up to 5 mm; Figures 2d and 2e). All three eclogites are foliated (S2), and the foliation is mainly formed by the SPO of omphacite as well as alternating kyanite/clinozoisite and omphacite-rich layers. Qualitatively, the foliation is most pronounced in N-059 and least pronounced in N-098 (Figures 2c–2e). The lineation of all three eclogites is formed by elongated minerals, mostly omphacite. All three samples show limited signs of retrogression (symplectites), along some grain boundaries (e.g., Figure 2d).

4.1.3. Retrogressed Eclogite (Sample N-010)

The sample is strongly retrogressed, preserving the eclogite-facies mineral assemblage only in patches (Figure 2f). It thus provides the opportunity to infer the effect of retrogression on the seismic velocities. Very fine grained symplectites (clinopyroxene, plagioclase, and quartz) make up >40 vol% of the rock. Relicts of the eclogite-facies assemblage include ~20 vol% omphacite, 15 vol% garnet, <10 vol% kyanite, <10 vol% clinozoisite, and minor quartz and phengite. The symplectites pseudomorph the eclogite-facies foliation, implying that the eclogite was strongly foliated before alteration (Figure 2f).

4.2. Samples for Thermodynamic Modeling

Samples were selected with the goal of covering a representative range of different granulite and eclogite varieties exposed on Holsnøy. All samples for which seismic velocities and CPO was measured were also used for thermodynamic modeling (see section 3.1 and Tables 1–3). Additional samples were analyzed with this method in order to constrain the range of velocities for the different rock types based on the variability of their mineral assemblages.

As described above, granulites are typically composed of up to 90 vol% plagioclase (~An_{50}), plus clinopyroxene (diopsidic to augitic) and garnet (pyrope rich). Minor phases include spinel, scapolite, rutile, and pyrite. Granulites are typically coarse grained (>5 mm), and the plagioclase grains have no SPO in the thin section. Garnet and clinopyroxene typically occur as flattened and elongated aggregates (coronas) that form the granulite-facies foliation (S1).

Eclogites are composed of omphacite and garnet (granulite-facies cores and newly grown almandine-rich rims). Garnet abundances are variable but usually high (up to 40 vol%). Additionally, the eclogites contain hydrous phases, that is, clinozoisite (X_{Ep} ~0.1) and low-celadonite phengite (Si ~3.25 p.f.u.). Eclogites typically also contain kyanite (5–15 vol%) and quartz (<10 vol%), and minor phases include apatite and pyrite. Eclogites, specifically those from shear zones, are foliated. The foliation is typically produced by omphacite, but also by kyanite and clinozoisite which are often aggregated in layers alternating with omphacite-rich layers. Further, eclogites are typically medium to fine grained.

5. Results

5.1. *P* and *S* Wave Velocities From Laboratory Measurements

In the lower-pressure range (up to ~250 MPa) the increase of the *P* and *S* wave velocities for all samples is steep and nonlinear, while it becomes moderate and nearly linear in the higher-pressure range (~250–600 MPa; Figure 3). While the strong increase in *P* and *S* wave velocities at lower pressure is typically attributed to the closure of cracks, the linear increase at higher pressure is considered to represent the characteristic pressure derivatives ($\delta V_P/\delta P$ and $\delta V_S/\delta P$, respectively) of the mineral aggregate. As expected, these pressure derivatives (for both *P* and *S* waves) are usually positive in all except two cases, where $\delta V_S/\delta P$ is slightly negative. The pressure derivatives allow extrapolation up to conditions realistic for the peak pressure-temperature conditions of the complex exposed on Holsnøy (700 °C and 2 GPa; e.g., Jamtveit et al., 1990).

Cracks that have been closed during pressurization do not reopen immediately during depressurization (hysteresis; e.g., Almqvist et al., 2013). Therefore, we used the measurements obtained during depressurization to calculate $\delta V_P/\delta P$ and $\delta V_S/\delta P$, because they better reflect the intrinsic rock properties (e.g., Mauler et al., 2000). The obtained linear fit was reviewed for each sample to verify that only measurements in the near-linear part were used. Additionally, in some measurements *P* and *S* wave velocities still increased at

Table 1
Laboratory Measurements of Anisotropic P Wave Velocities of Granulites and Eclogites

Sample	Direction	V_P (km/s) Measured	V_P (km/s) Extrapolated	$\delta V_P/\delta P$ ($\times 10^{-4}$ km s^{-1} MPa^{-1})	$\delta V_P/\delta T$ ($\times 10^{-4}$ km s^{-1} °C^{-1})	A_{VP} (%) Measured	A_{VP} (%) Extrapolated
Granulites							
N-058A[a]	x	6.86	6.99 ± 0.03	1.01 ± 0.10	−1.59 ± 0.28	1	2
	y	6.92	7.00 ± 0.04	0.48 ± 0.17	−2.92 ± 0.41		
	z	6.83	7.12 ± 0.05	2.13 ± 0.21	−1.92 ± 0.34		
N-058B[a]	x	7.10	7.26 ± 0.03	1.27 ± 0.12	−1.95 ± 0.21	5	5
	y	6.73	6.90 ± 0.04	1.09 ± 0.15	−2.58 ± 0.37		
	z	6.85	7.11 ± 0.05	1.90 ± 0.22	−2.10 ± 0.39		
N-103	x	7.20	7.46 ± 0.05	2.28 ± 0.20	−3.69 ± 0.36	2	5
	y	7.11	7.35 ± 0.06	1.76 ± 0.24	−4.06 ± 0.72		
	z	7.24	7.76 ± 0.08	3.80 ± 0.37	−3.10 ± 0.51		
Eclogites							
N-059[a]	x	8.18	8.45 ± 0.05	2.48 ± 0.21	−3.08 ± 0.30	11	9
	y	7.61	7.87 ± 0.08	2.02 ± 0.35	−4.76 ± 0.49		
	z	7.33	7.74 ± 0.11	3.06 ± 0.51	−3.84 ± 0.44		
N-098	x	8.12	8.39 ± 0.07	1.31 ± 0.12	−2.34 ± 1.06	9	9
	y	7.73	7.85 ± 0.03	0.50 ± 0.04	−5.18 ± 0.53		
	z	7.40	7.68 ± 0.09	1.95 ± 0.44	−4.06 ± 0.46		
N-101	x	8.31	8.63 ± 0.06	2.45 ± 0.30	−4.25 ± 0.25	7	8
	y	7.89	8.00 ± 0.03	0.58 ± 0.04	−4.42 ± 0.53		
	z	7.73	8.01 ± 0.08	2.14 ± 0.37	−4.39 ± 0.55		
Retrogressed eclogite							
N-010[a]	x	7.40	7.55 ± 0.02	1.36 ± 0.06	−2.36 ± 0.25	3	3
	y	7.17	7.36 ± 0.05	1.41 ± 0.20	−3.84 ± 0.41		
	z	7.15	7.52 ± 0.08	2.81 ± 0.36	−3.94 ± 0.36		

Note. Corresponding pressures and temperatures are 600 MPa and 600 °C (measured) and at 2 GPa and 700 °C (extrapolated).
[a]Measured values from Motra and Zertani (2018).

the beginning of depressurization of the sample, before reaching a linear decrease. These measurements were also excluded from the linear fit.

The slope and *y*-intercept that were obtained from this procedure were then used to extrapolate the velocity measurements to 2 GPa and 700 °C (Tables S5 and S7). The uncertainty of the extrapolation far exceeds the uncertainty of the measurement itself. Therefore, we computed the standard error for each extrapolated value from the standard error of the slope and *y*-intercept of our linear fit. The results are shown in Tables 1 and 2.

Both *P* and *S* wave velocities decrease linearly with increasing temperature. Analogously to the pressure derivatives, the temperature derivatives ($\delta V_P/\delta T$ and $\delta V_S/\delta T$, respectively) can be used to extrapolate the measured velocities to peak pressure-temperature conditions.

In the following all results for *P* and *S* wave velocities refer to the results after extrapolation to 2 GPa and 700 °C, unless stated otherwise. *P* and *S* wave velocities from laboratory measurements of both granulites and eclogites are summarized in Tables 1 and 2 and Figure 4; the complete measurements are provided in Tables S8 to S14. Note that the results from samples N-010, N-058A, N-058B, and N-059 have been previously discussed in a geomechanical context in Motra and Zertani (2018).

P wave velocities averaged over the three propagation directions range from 6.87 to 7.18 km/s for granulites and 7.71 to 7.98 km/s for eclogites. The range of mean *S* wave velocities is 3.67 to 4.01 km/s in granulites and 4.51 to 4.59 km/s for eclogites. Sample N-010, with significant retrogression, has a mean *P* wave velocity of 7.24 km/s and a mean *S* wave velocity of 4.24 km/s.

5.2. *P* and *S* Wave Velocities From Thermodynamic Modeling

The mineral assemblages predicted by the thermodynamic calculations are consistent with the eclogite and granulite varieties exposed on Holsnøy. The calculations yield mineral assemblages in the range of 47–77 vol% plagioclase + 12–46 vol% garnet + 3–7 vol% clinopyroxene ± orthopyroxene ± spinel ± ilmenite for

Table 2
Laboratory Measurements of Anisotropic S Wave Velocities of Granulites and Eclogites

		V_S (km/s)		$\delta V_S/\delta P$ ($\times 10^{-4}$ km s^{-1} MPa^{-1})	$\delta V_S/\delta T$ ($\times 10^{-4}$ km s^{-1} °C^{-1})	A_{pol} (%)	
Sample	Direction	Measured	Extrapolated			Measured	Extrapolated
Granulites							
N-058A[a]	yx	3.65	3.68 ± 0.02	0.16 ± 0.04	−1.26 ± 0.22	1	1
	zx	3.68	3.70 ± 0.01	0.05 ± 0.02	−0.81 ± 0.16		
	xy	3.69	3.75 ± 0.02	0.24 ± 0.06	−1.67 ± 0.29	3	3
	zy	3.58	3.62 ± 0.01	0.13 ± 0.03	−1.57 ± 0.18		
	xz	3.69	3.75 ± 0.02	0.22 ± 0.07	−1.03 ± 0.28	0	0
	yz	3.70	3.77 ± 0.02	0.26 ± 0.05	−1.09 ± 0.38		
N-058B[a]	yx	3.77	3.74 ± 0.02	−0.29 ± 0.06	−1.23 ± 0.19	1	2
	zx	3.74	3.80 ± 0.03	0.37 ± 0.12	−1.59 ± 0.33		
	xy	3.70	3.73 ± 0.02	0.17 ± 0.04	−2.18 ± 0.31	2	3
	zy	3.77	3.83 ± 0.02	0.33 ± 0.03	−1.95 ± 0.30		
	xz	3.81	3.88 ± 0.03	0.30 ± 0.09	−1.39 ± 0.36	1	1
	yz	3.76	3.83 ± 0.02	0.36 ± 0.07	−0.74 ± 0.27		
N-103	yx	4.17	4.31 ± 0.02	1.08 ± 0.06	−1.40 ± 0.17	2	2
	zx	4.10	4.24 ± 0.05	0.78 ± 0.20	−3.29 ± 0.56		
	xy	3.89	4.08 ± 0.04	1.30 ± 0.13	−2.87 ± 0.41	0	2
	zy	3.90	4.00 ± 0.03	0.67 ± 0.05	−3.18 ± 0.42		
	xz	4.00	4.12 ± 0.03	0.81 ± 0.11	−1.44 ± 0.33	0	1
	yz	4.01	4.18 ± 0.03	1.16 ± 0.11	−1.80 ± 0.40		
Eclogites							
N-059[a]	yx	4.62	4.73 ± 0.03	0.94 ± 0.13	−1.42 ± 0.20	2	1
	zx	4.53	4.70 ± 0.03	1.31 ± 0.14	−1.62 ± 0.17		
	xy	4.57	4.77 ± 0.05	1.52 ± 0.20	−2.77 ± 0.29	4	5
	zy	4.40	4.54 ± 0.03	1.07 ± 0.13	−2.96 ± 0.23		
	xz	4.44	4.58 ± 0.04	1.09 ± 0.20	−1.77 ± 0.33	1	1
	yz	4.47	4.64 ± 0.04	1.24 ± 0.16	−2.16 ± 0.30		
N-098	yx	4.72	4.69 ± 0.03	−0.26 ± 0.06	−3.36 ± 0.48	1	0
	zx	4.65	4.71 ± 0.03	0.33 ± 0.06	−3.44 ± 0.47		
	xy	4.47	4.54 ± 0.02	0.34 ± 0.06	−3.74 ± 0.29	3	3
	zy	4.35	4.42 ± 0.02	0.31 ± 0.09	−3.63 ± 0.25		
	xz	4.55	4.68 ± 0.04	0.61 ± 0.18	−1.74 ± 0.26	0	0
	yz	4.56	4.71 ± 0.02	0.87 ± 0.11	−1.59 ± 0.15		
N-101	yx	4.77	4.76 ± 0.03	0.18 ± 0.07	−4.03 ± 0.36	3	2
	zx	4.61	4.65 ± 0.03	0.37 ± 0.05	−4.61 ± 0.39		
	xy	4.58	4.63 ± 0.02	0.46 ± 0.04	−3.36 ± 0.33	2	2
	zy	4.48	4.53 ± 0.02	0.48 ± 0.08	−3.31 ± 0.24		
	xz	4.56	4.64 ± 0.03	0.45 ± 0.09	−1.87 ± 0.35	0	0
	yz	4.54	4.66 ± 0.03	0.83 ± 0.12	−2.16 ± 0.43		
Retrogressed eclogite							
N-010[a]	yx	4.29	4.34 ± 0.02	0.42 ± 0.10	−1.07 ± 0.18	1	1
	zx	4.26	4.29 ± 0.02	0.29 ± 0.07	−1.32 ± 0.16		
	xy	4.24	4.32 ± 0.02	0.68 ± 0.10	−1.88 ± 0.09	1	1
	zy	4.20	4.26 ± 0.02	0.52 ± 0.08	−2.12 ± 0.21		
	xz	4.17	4.28 ± 0.03	0.77 ± 0.13	−1.49 ± 0.28	3	3
	yz	4.28	4.39 ± 0.03	0.85 ± 0.13	−1.71 ± 0.25		

Note. Corresponding pressures and temperatures are 600 MPa and 600 °C (measured) and at 2 GPa and 700 °C (extrapolated).
[a]Measured values from Motra and Zertani (2018).

granulites and 37–53 vol% omphacite + 7–37 vol% garnet + 4–19 vol% kyanite + 2–9 vol% phengite + <1 vol% rutile ± amphibole ± zoisite ± quartz for eclogites (Figure 5 and Table S15).

Since the eclogites are formed during continuous fluid infiltration (Austrheim, 1987), the calculations were done with H_2O in excess, potentially introducing the problem that the abundance of hydrous phases calculated is unrealistically high as no metastability or chemical subdomain is preserved during this bulk equilibrium approach. However, the resulting H_2O content from the calculations is 0.2–1.2 wt% (Table 3), which is in good agreement with the loss on ignition obtained from XRF analysis.

Table 3
P and S Wave Velocities Calculated Using Thermodynamic Modeling for Eclogites and Granulites

Sample	V_P (km/s)	$\delta V_P/\delta P$ ($\times 10^{-4}$ km s^{-1} MPa^{-1})	$\delta V_P/\delta T$ ($\times 10^{-4}$ km s^{-1} °C^{-1})	V_S (km/s)	$\delta V_S/\delta P$ ($\times 10^{-4}$ km s^{-1} MPa^{-1})	$\delta V_S/\delta T$ ($\times 10^{-4}$ km s^{-1} °C^{-1})	H_2O (wt%)
Granulites							
H001	7.06	1.50	−4.35	3.96	1.05	−2.56	—
N-044	7.50	1.10	−4.27	4.21	0.67	−2.43	—
N-058	6.93	1.61	−4.32	3.87	1.15	−2.54	—
N-079	7.20	1.37	−4.32	4.03	0.92	−2.44	—
N-080	7.20	1.38	−4.30	4.03	0.94	−2.45	—
N-084	7.40	1.21	−4.29	4.15	0.77	−2.41	—
N-102	7.27	1.31	−4.30	4.07	0.87	−2.44	—
N-103	7.37	1.23	−4.29	4.13	0.79	−2.40	—
Eclogites							
N-005	8.17	0.74	−3.34	4.66	0.30	−1.53	0.3
N-010	7.96	0.81	−3.87	4.58	0.24	−1.40	0.2
N-030	7.97	0.80	−3.65	4.58	0.26	−1.42	0.3
N-037	7.92	0.83	−3.84	4.57	0.24	−1.33	0.3
N-043	7.71	0.89	−4.26	4.47	0.24	−1.60	0.5
N-045	8.00	0.77	−3.49	4.58	0.29	−1.49	0.4
N-046	8.10	0.76	−4.02	4.63	0.31	−2.19	0.3
N-052	7.73	0.79	−3.92	4.36	0.33	−2.58	1.2
N-054	8.03	0.78	−3.64	4.62	0.27	−1.38	0.3
N-059	7.99	0.82	−3.87	4.61	0.25	−1.36	0.2
N-073	7.93	0.81	−3.61	4.57	0.26	−1.33	0.4
N-094	7.92	0.82	−4.00	4.56	0.33	−2.10	0.5
N-098	8.01	0.80	−3.77	4.62	0.27	−1.38	0.2
N-101	8.03	0.79	−3.97	4.60	0.34	−2.21	0.5

Note. The displayed velocities for granulites are extrapolated to 2 GPa and 700 °C based on the calculated pressure and temperature derivatives.

P and *S* wave velocities calculated using thermodynamic modeling (Table 3) agree well with those from laboratory measurements (Figure 4): *P* wave velocities range from 6.93 to 7.50 km/s, and *S* wave velocities range from 3.87 to 4.21 km/s. *P* and *S* wave velocities for eclogites range from 7.71 to 8.17 and 4.36 to 4.66 km/s, respectively.

5.3. Seismic Anisotropy and V_P/V_S Ratios

Since laboratory measurements provide seismic velocities in three perpendicular directions of the rock volume, they can be used to calculate the respective seismic anisotropy. *P* wave anisotropy is calculated by

$$A_{V_P} = \frac{(V_{P\text{max}} - V_{P\text{min}})}{(V_{P\text{mean}})} * 100$$

P wave anisotropy ranges from 2% to 5% for granulites and is up to 8% to 9% for eclogites. In all three eclogite samples, the fast axis is parallel to the stretching lineation (*x*), and the slowest axis is perpendicular to the foliation (*z*; Table 1). In the granulite samples, however, there is no consistent relationship between anisotropy and the *x*, *y*, and *z* axes. *P* wave anisotropy in the retrogressed eclogite is 3%.

The *S* wave anisotropy between the two orthogonally polarized waves within one propagation direction is calculated from

$$A_{\text{pol}} = \frac{V_{\text{SF}} - V_{\text{SS}}}{V_{\text{Smean}}} * 100$$

where V_{SF} is the *S* wave velocity in the fast polarization direction and V_{SS} is the *S* wave velocity in the slow polarization direction. This results in three values for anisotropy, one for every propagation direction (Table 2). For granulites they range from 0% to 3%, and for eclogites they range from 0% to 5%. The retrogressed eclogite has *S* wave anisotropies of 1–3%.

V_P/V_S ratios from thermodynamic modeling are in the range from 1.72 to 1.77 for eclogites and 1.78 to 1.79 for granulites (Figure 4b). Those obtained from laboratory measurements (calculated from the mean *P* and *S* wave velocities) are more variable. Granulites have V_P/V_S ratios of 1.81 to 1.90 and eclogites range from 1.72
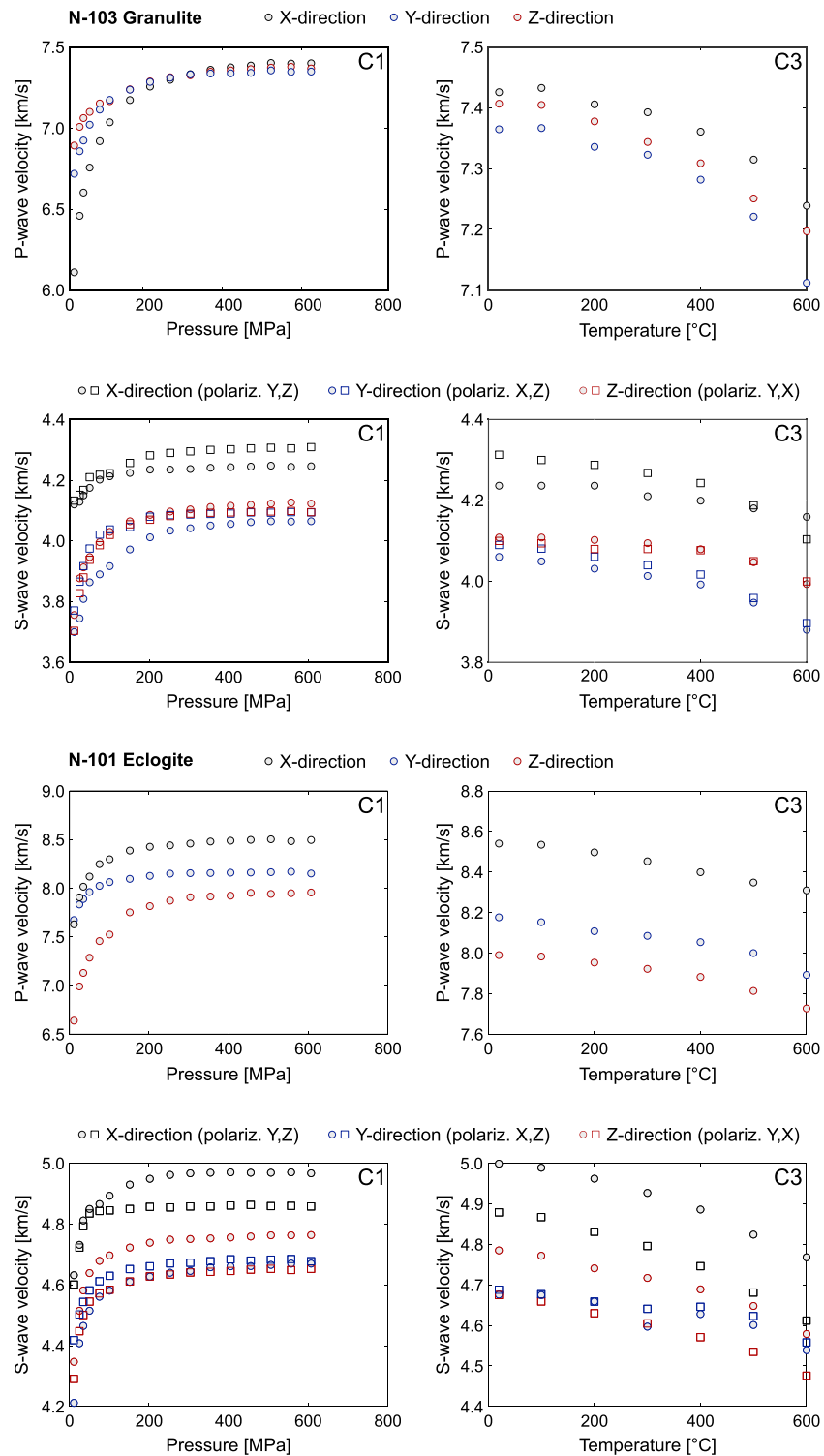
Figure 3. Results from laboratory measurements of samples N-103 (granulite) and N-101 (eclogite) shown as examples to illustrate the general qualitative trend typical for seismic velocity measurements. (left) *P* and *S* wave velocities increase steeply and nonlinearly at lower pressures before they trend along a much shallower, nearly linear slope. (right) Seismic velocities decrease linearly with increasing temperature. C1 and C3 refer to the measurement cycles 1 and 3, respectively (see main text for details).
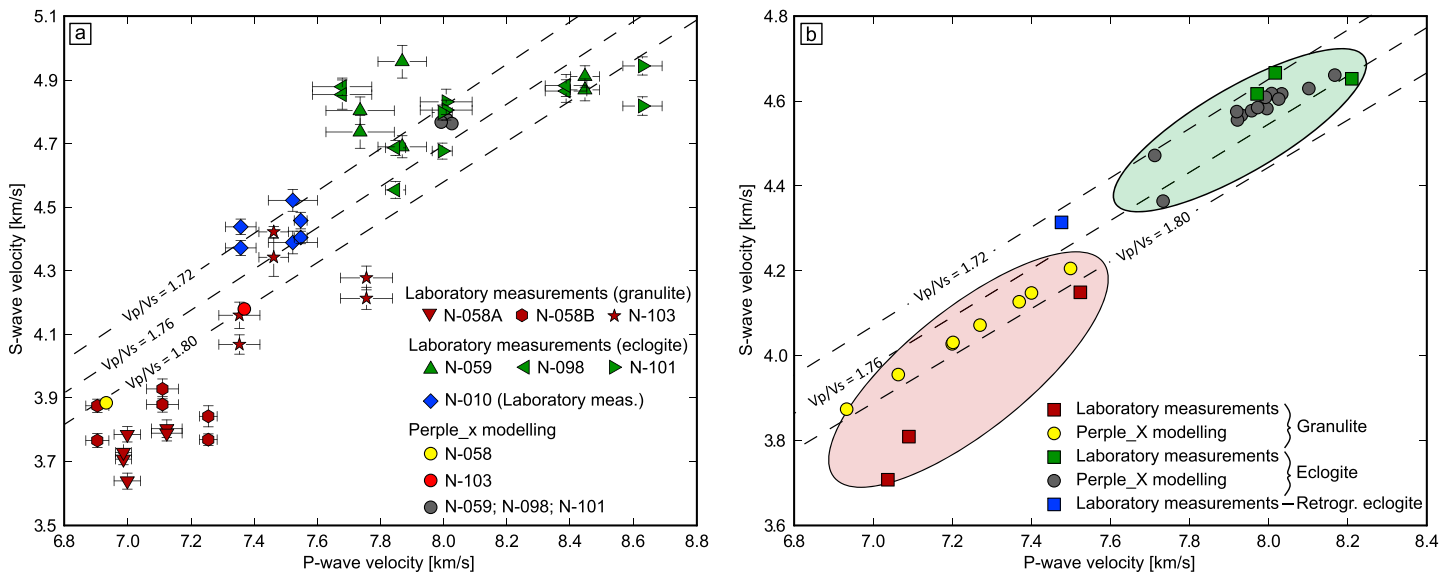
Figure 4. *P* and *S* wave velocities from laboratory measurements and thermodynamic modeling. (a) *S* wave versus *P* wave velocity diagram showing the results from laboratory measurements for each of the measurement directions. Note that each pair of *S* wave velocities was plotted against one *P* wave velocity as there are two *S* wave velocities per propagation direction (*x*, *y*, and *z*). The spread of velocities in different directions corresponds to the seismic anisotropy. Additionally, the diagram gives the results obtained from thermodynamic modeling for the same samples (circles). The dashed lines indicate V_P/V_S ratios. (b) *S* wave velocity versus *P* wave velocity diagram showing results from thermodynamic modeling (circles). Additionally, laboratory measurement results are shown as averages for each sample over the three directions. The red and green areas show the range of isotropic granulite and eclogite velocities, respectively.

to 1.77. The retrograded eclogite has a V_P/V_S ratio of 1.73. Additionally, a directional dependence of the V_P/V_S ratio can be deduced from the laboratory measurements (Figure 4a). In granulites, V_P/V_S ratios vary by 0.01–0.12 within one sample, while they vary by 0.11–0.15 in eclogites and by 0.03 in the retrogressed eclogite.

5.4. Crystallographic Preferred Orientations

TOF neutron diffraction provides the opportunity to estimate CPO for sample volumes that are significantly larger than those analyzed using other methods (e.g., EBSD). In this study we retrieved the CPO of two granulite and two eclogite samples. Figure 6 shows the pole figures of plagioclase and clinopyroxene. The CPO of other phases can be found in the supporting information (Figure S2).

In granulites the CPO of plagioclase appears to be weak (Figures 6a and 6b). While plagioclase in N-103 seems to be oriented almost randomly, in N-058 it has moderate CPO. The [001]-axis (N-058) of plagioclase is preferentially aligned along *y*, and the [010]-pole is preferentially oriented parallel to *z* (Figure 6a). Clinopyroxene and garnet in granulites show no CPO.

In eclogites (Figures 6e and 6f), omphacite CPO is strong with the [001]-axes subparallel to *x* and the [010]-pole along *z*. This holds true for both eclogite samples analyzed in this study, with CPO in N-059 being slightly more pronounced. Quartz and clinozoisite CPO, on the other hand, are negligible, and garnet has no CPO.

6. Discussion

### 6.1. The Effect of Eclogitization and Deformation on Seismic Properties

To decipher how eclogitization modifies the petrophysical properties of the crust during deep burial in an incipient continental collision, we employed two methods to ascertain the changes of seismic properties resulting from the granulite-to-eclogite transition on Holsnøy. First of all, we note that the velocities measured in the lab and calculated from thermodynamic modeling generally agree well (Figure 4b). The most apparent difference between velocities from eclogites and granulites is an increase of the *P* and *S* wave velocity by ~0.8 and ~0.6 km/s, respectively (Figure 4a). *P* and *S* wave velocities of granulite samples at granulite-facies conditions (~0.05 km/s slower than those at eclogite-facies conditions) are in agreement with representative mid to lower crustal velocities (e.g., Almqvist & Mainprice, 2017; Kern et al., 1996; Lloyd, Butler,
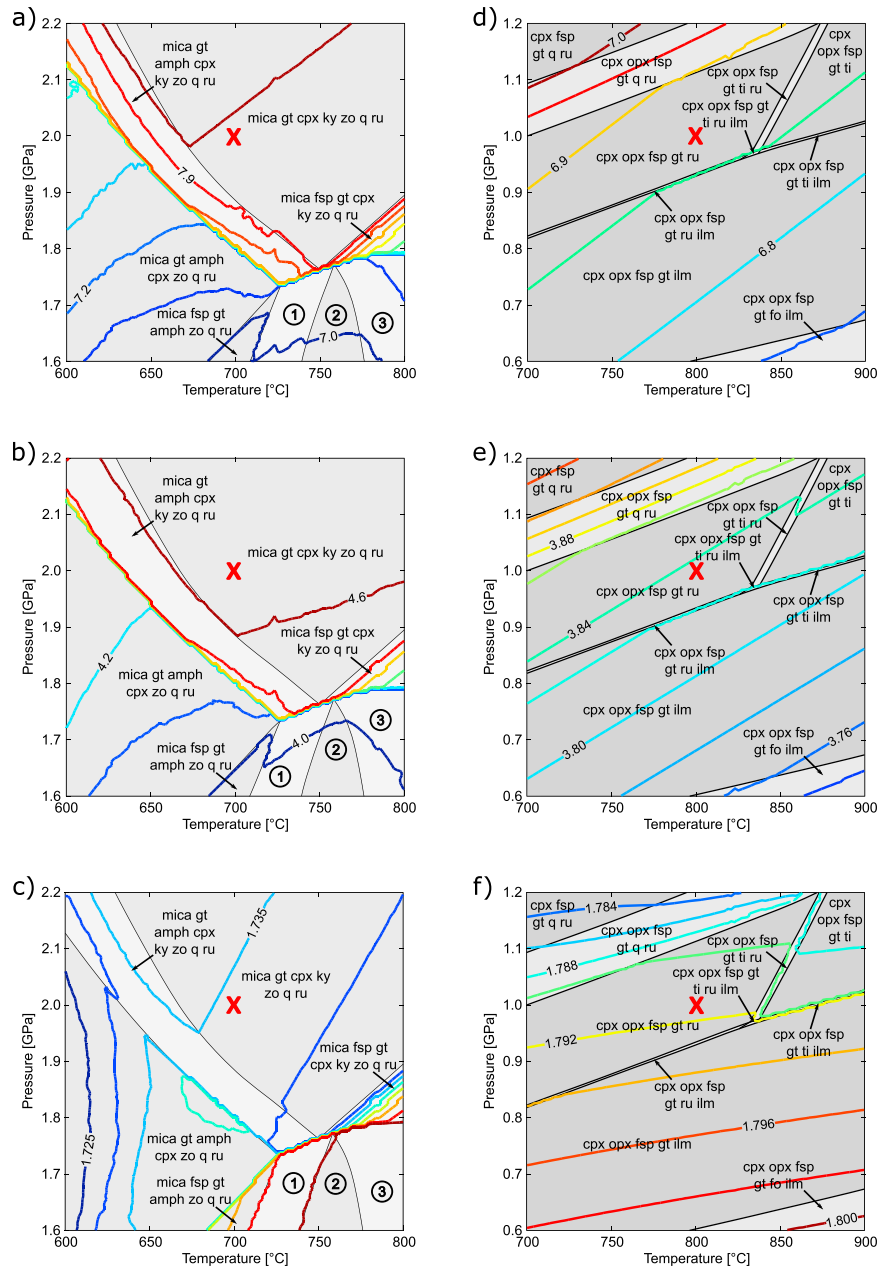
Figure 5. Pseudosection results of (a–c) one eclogite sample (N-059) and (d–f) one granulite sample (N-058). The overlying contours show how (a and d) *P* wave velocity, (b and e) *S* wave velocity, and (c and f) V_P/V_S ratio vary throughout the relevant pressure and temperature space. In (a)–(c), mineral assemblages at low pressure and high temperature (lower right corner) are referred to by the following: (1) mica + fsp + gt + amph + ky + zo + q + ru, (2) mica + fsp + gt + amph + zo + q + ru, and (3) mica + fsp + gt + amph + cpx + zo + q + ru. The red X marks the *P-T* conditions at which *P* and *S* wave velocities were extracted. Abbreviations: fsp = feldspar; gt = garnet; amph = amphibole; ky = kyanite; zo = zoisite; q = quartz; ru = rutile; cpx = clinopyroxene; opx = orthopyroxene; fo = forsterite; sph = titanite; ilm = ilmenite.

et al., 2011). This significant velocity contrast between the eclogite-facies shear zones and the metastable granulite-facies protolith at eclogite-facies conditions suggests that depending on scale they should be detectable using geophysical methods such as the receiver function method (Kind et al., 2012).

Previously, Fountain et al. (1994) reported *P* wave velocities from laboratory measurements of the granulites and eclogites from Holsnøy. The reported velocities are systematically higher than the ones presented here, which most likely results from the measurement setup that did not include measuring the velocities at elevated temperatures; an increase in temperature typically results in a decrease in *P* wave velocity (e.g., Kern,
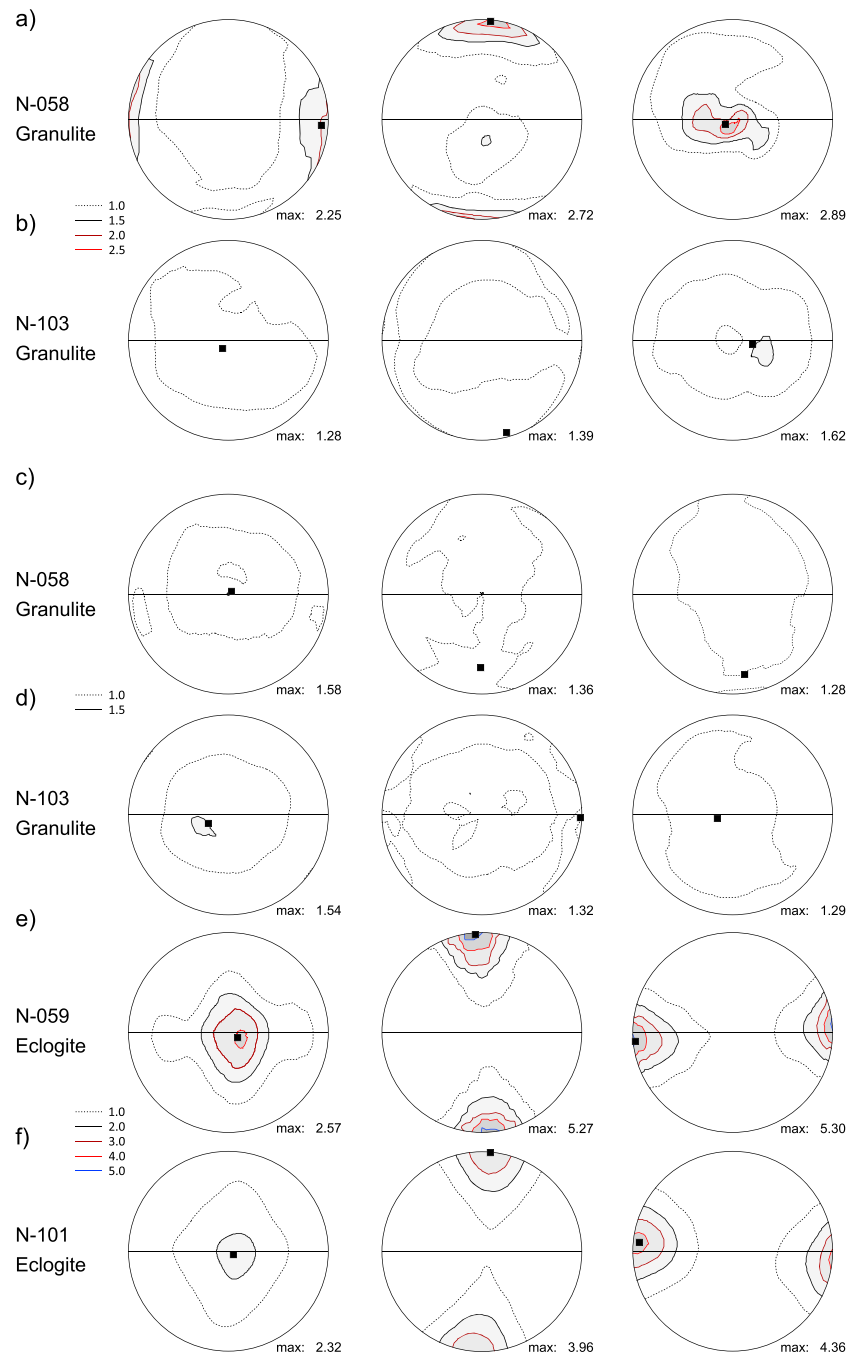
Figure 6. Pole figures showing crystallographic preferred orientation of (a and b) plagioclase and (c–f) clinopyroxene. Pole figures are equal area projections (lower hemisphere) on a 5 × 5° grid. The horizontal line corresponds to the foliation (*xy*-plane) and the lineation is EW. Contours are multiples of a random distribution and maximum densities are given for each plot (lower right and square).

1978). Additionally, Bascou et al. (2001) calculated seismic velocities from EBSD measurements for one eclogite sample from Holsnøy that also has a *P* wave velocity higher than the ones we report here. Whether the higher *P* wave velocity of this single measurement is caused by a seismically faster mineral assemblage of that particular sample or because the calculation from EBSD measurements does not include fractures and grain boundaries, which are included in laboratory velocity measurements and generally act to decrease the resulting *P* wave velocity, is difficult to assess. In any case, eclogitization of lower crustal granulites results in a significant increase of the seismic velocities of the affected rocks.

One of the advantages of measuring velocities using the ultrasonic pulse transmission technique is that they are related to the principal fabric directions of the studied sample (Figures 3 and 4a), providing the opportunity to calculate the seismic anisotropy. This is of particular interest because many geophysical studies use seismic anisotropy in combination with seismic velocity models to identify lithologies and reconstruct deformation history at depth (e.g., Dreiling et al., 2018; Olive et al., 2014).

P wave anisotropy of the granulites studied here is low (2–5%; Figure 4a), although plagioclase, which makes up most of the rock volume, has a high intrinsic seismic anisotropy (Almqvist & Mainprice, 2017; Brown et al., 2006, 2016). However, Almqvist and Mainprice (2017) pointed out that plagioclase-rich rocks often have a low seismic anisotropy because of the lack of plagioclase CPO which agrees with our results. Samples N-058A and N-058B are two subsamples of the same sample, with N-058B containing a higher amount of pyroxene and garnet. Regardless, their *P* wave anisotropy varies distinctly (N-058A: 2% and N-058B: 5%). As shown in Figure 6, N-058 has a weak but distinct CPO of plagioclase. In N-058B, the CPO-induced *P* wave anisotropy is amplified by the ~10 vol% higher amount of pyroxene-garnet aggregates, which are flattened in the foliation plane and often elongated parallel to the lineation (*x*). In N-058A, however, where these aggregates are less abundant, the remaining anisotropy is colinear with the plagioclase CPO. Here the fast propagation direction is parallel to [010] and the *z*-axis (Figure 6). This axis is the one that varies least between the two aliquots, and the increased velocity in the *x* and *y* directions is therefore solely the result of the higher amount of pyroxene-garnet aggregates. Sample N-103, on the other hand, has a *P* wave anisotropy, similar to that of N-058B. In this sample, crystallographic orientations of all phases seem to be almost random and can thus not explain the *P* wave anisotropy. This suggests that here the anisotropy is caused by the alignment of the garnet-pyroxene aggregates themselves; that is, anisotropy here appears to be dominated by SPO.

The eclogites we report here have a significantly higher *P* wave anisotropy than expected. *P* wave anisotropy of eclogite typically reported in the literature is in the range of 1–7% (e.g., Bascou et al., 2001; Fountain et al., 1994). The highest *P* wave anisotropy we obtained from laboratory measurements, however, was 9% (Figure 4 and Table 1). Our results are supported by the CPO measurements presented in Figures 6e and 6f. Omphacite shows a strong CPO with the [001]-axes parallel to the lineation and subsequently the fast *P* wave propagation direction. The slow *P* wave propagation direction is parallel to both the foliation pole (*z*) and [010]. The orientation of fast and slow *P* wave propagation directions with respect to crystallographic axes is consistent with the single-crystal properties of omphacite (Bascou et al., 2001), suggesting that the development of omphacite CPO in the eclogites exposed on Holsnøy significantly contributed to the high seismic anisotropy (Figure 6). This is supported by the anisotropy obtained from the retrogressed eclogite (N-010). Here omphacite has been largely replaced by symplectites that pseudomorph the previous fabric, mimicking the previously pronounced SPO, while the CPO of omphacite has been erased. This replacement results in a significantly lower (1–3%) *P* wave anisotropy, suggesting that omphacite CPO in the nonretrogressed eclogites dominates the seismic anisotropy. In summary, eclogitization coeval with texture development has the potential to enhance the seismic anisotropy to anomalously high values of 9% compared to typical eclogite anisotropy (e.g., Fountain et al., 1994; Keppler et al., 2017; Kern et al., 1999; Worthington et al., 2013), including those from Holsnøy, where prior to our measurements a maximum anisotropy of 7% had been reported (Bascou et al., 2001; Fountain et al., 1994).

When using Holsnøy as an analog for deeply buried lower crust, it has to be noted that not all eclogites on Holsnøy are formed in shear zones. It was pointed out recently that large (up to 2 km in diameter) eclogitized domains on Holsnøy are not related to deformation processes but that in some areas metamorphism is dominated by static, fluid-induced eclogite-facies reequilibration (Jamtveit et al., 2000; Zertani et al., 2019). In combination with the low seismic anisotropy of the granulites, this suggests that in low-strain domains *P* wave anisotropy will be low (likely <5%). Although the three eclogites analyzed here are all from an eclogite shear zone, the results support this interpretation because the sample with the most pronounced foliation (N-059) also has the highest anisotropy and the sample with the least pronounced foliation (N-098) also has the lowest anisotropy. Hence, seismic anisotropy in eclogites is strongly dependent on the dominant eclogitization mechanism. Subsequently, in order to use seismic anisotropy as a characteristic property to detect eclogite occurrences at depth, the geological setting and the structural framework have to be considered carefully.

Another important characteristic used to study rocks at depth is the V_P/V_S ratio, which is of specific interest in receiver function imaging, because this method is based on the differences in arrival times of converted

waves at boundaries with contrasting seismic velocities (Kind et al., 2012). Additionally, the V_P/V_S ratio is often used to extract lithological information of the rocks at depth or to detect the presence of fluids (e.g., Bloch et al., 2018; Zhang et al., 2004).

The granulites and eclogites studied here both have low to medium V_P/V_S ratios. Although the difference is small, the two groups can be clearly distinguished (Figure 4b). Granulites have V_P/V_S ratios >1.78, while the V_P/V_S ratio of eclogites is ~1.74. This means that eclogitization, at least as it proceeded in the Lindås nappe, results in a decrease of the V_P/V_S ratio by 0.04–0.06. In eclogites from the Western Gneiss Region (Norway) Worthington et al. (2013) report V_P/V_S ratios of 1.75–1.78, which is higher than the eclogites reported here but still consistently below the values obtained from the granulites. The anomalously high V_P/V_S ratios of samples N-058A and N-058B obtained from laboratory measurements, however, are likely not representative of granulite-facies rocks because their S wave velocities are probably reduced by the significant zoisite formation due to rehydration, which possibly even increases the difference between V_P/V_S ratios of the (partially rehydrated) granulite prior to eclogitization.

The V_P/V_S ratio reduction from granulite to eclogite is due to the replacement of plagioclase. This is particularly interesting because plagioclase is the most abundant mineral in the continental crust with typical V_P/V_S ratios of 1.82–1.86 (Christensen, 1996). As the granulites studied here are derived from anorthosites, it is not surprising that their V_P/V_S ratio is similar to that of plagioclase. With the breakdown of plagioclase, the influence of pyroxene (omphacite) and garnet on the bulk seismic properties increases significantly. Since both pyroxene and garnet have lower V_P/V_S ratios (e.g., almandine ~1.79 and jadeite ~1.74; Christensen, 1996), this change of mineral assemblage reduces the bulk V_P/V_S ratio. Additionally, the seismic anisotropy of the rocks also implies a directional dependence of the V_P/V_S ratios. In summary, eclogitization of lower continental crust, accompanied by shear zone formation, causes (1) increased seismic velocities, (2) increased seismic anisotropy, and (3) decreased V_P/V_S ratios.

6.2. Implications for the Detection of Eclogite-Facies Shear Zones at Depth Using Large-Scale Geophysical Imaging

Structures at depth can only be imaged using active and passive seismic methods if they are sufficiently large to be detected using the frequencies typically employed in such studies and if they have seismic properties that vary from those of the adjacent rocks (e.g., Mooney & Meissner, 1992; Rondenay et al., 2005). It has been shown recently that the general structure of the shear zones on Holsnøy is qualitatively scale independent as there is a gradient of strain and eclogite abundance from the center of shear zones outward, regardless of the shear zone scale (Zertani et al., 2019), suggesting that the same structural framework on a larger scale could be present at depth in a subduction/collision setting actively deforming and eclogitizing previously metastable crustal rocks.

To illustrate this, Figure 7 shows simplified models of three of the main shear zones on Holsnøy with corresponding P and S wave velocities and the resulting V_P/V_S ratios as well as normal incidence P wave reflection coefficients (A_1/A_0) calculated from

$$\frac{A_1}{A_0} = \frac{\rho_2 * V_{P_2} - \rho_1 * V_{P_1}}{\rho_2 * V_{P_2} + \rho_1 * V_{P_1}}$$

where ρ_1 and ρ_2 are the densities and V_{P_1} and V_{P_2} are the P wave velocities below and above the boundary, respectively (Fowler, 2005). P and S wave velocities were taken from the mean values presented in this study (Figure 4b). These models show that in general the granulite-to-eclogite transition produces a significant contrast in these parameters (seismic velocities, etc.) between the unaltered granulite, the eclogite breccia, and the eclogite shear zones, which are useful for seismic imaging.

Similar models for Holsnøy have been shown by Fountain et al. (1994) for P waves only. They concluded that although these shear zones are at the lower end of what could be imaged in terms of shear zone thickness, such structures could be detectable at depth. Their study, however, did not fully take the transitional nature of the eclogite breccia into account. The eclogite breccia provides both a petrological and a structural transition between the two end-members, which can be more than a few hundred meters thick (Zertani et al., 2019). Hence, the variation of seismic properties is also gradual. For this reason, we introduced simple linear gradients throughout the shear zones that reflect the gradually decreasing abundance of eclogite away from
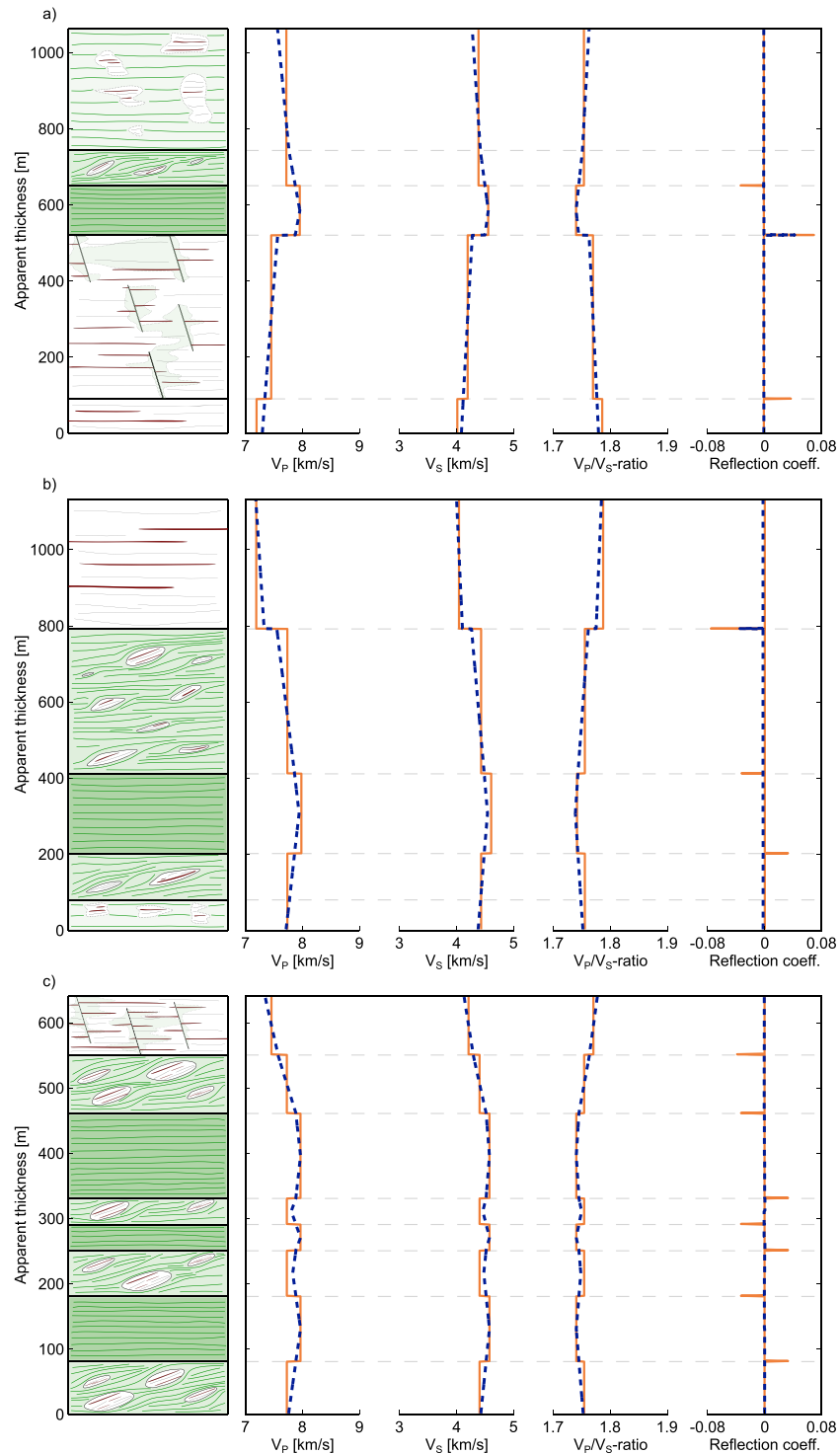
Figure 7. Diagrams showing how (isotropic) *P* and *S* wave velocities and V_P/V_S ratios vary within major shear zones on Holsnøy and the resulting reflection coefficients. (left) Shear zone thickness is from Zertani et al. (2019). The three examples depicted are (a) the Upper Eldsfjellet shear zone, (b) the Skurtveit shear zone, and (c) the Hundskjeften shear zone. End-member *P* and *S* wave velocities were chosen as follows: granulite: 7.19 (*P* wave) and 4.00 km/s (*S* wave); eclogite: 7.96 (*P* wave) and 4.57 km/s (*S* wave). The solid line in each diagram shows the variation assuming a fixed value for the transitional layers. Those were set to 70% eclogite (eclogite breccia) and 35% eclogite (granulite with minor shear zones and small-scale static eclogite features; see Zertani et al., 2019, for detailed descriptions). The dashed lines show the variation when assuming linear changes between the different rock types. Here eclogite abundances were chosen as follows: eclogite (90–100%), deformed and undeformed eclogite breccia (50–90%), granulite with minor eclogitization features (20–50%), and granulite (0–20%). All mixtures between eclogite and granulite were calculated as Voigt-Reuss-Hill averages (Hill, 1952).

the shear zone center (Figure 7), by defining eclogite abundances in the center and the boundaries of each of the layers in agreement with the classification discussed in Zertani et al. (2019). The resulting *P* and *S* wave velocities are calculated as Voigt-Reuss-Hill averages (Hill, 1952). Here it is evident that the contrast of, for example, *P* and *S* wave velocities from the granulite to the eclogite is typically not sharp but that they cause a smooth transition from lower to higher seismic velocities and vice versa (Figure 7), making the detection of such structures potentially more difficult, especially in combination with the limited shear zone thickness. Only in rare cases a sharp contrast is retained. This is not because the transition zone in those areas is missing but because the thickness of this zone is below the scale mapped by Zertani et al. (2019). This is consistent with results from a mid to upper crustal shear zone studied by Rey et al. (1994), where an increased thickness of such a transition zone results in decreased reflection coefficients.

To assess these effects semiquantitatively, we calculated the normal incidence *P* wave reflection response of these shear zone structures with the reflectivity method (Fuchs & Müller, 1971) in the implementation by Sandmeier and Wenzel (1986) for both the models with the sharp boundaries and (more realistic) smooth transitions. In order to suppress high-frequency artifacts inherent to the reflectivity method and to judge the frequency response, we convolved the response with Ricker wavelets of 20 and 5 Hz dominant frequency (Figure 8), as might be encountered in a high-resolution crustal reflection survey or a wide-angle crustal-scale profile or records from a local earthquake, respectively. As expected, the details of the transitions in the shear zone have a stronger influence on the waveform at higher frequencies, but nevertheless, even at 5 Hz for at least one of the shear zone models, distinctly different responses are seen for the smooth and sharp transitions. The smooth transition models usually seem to be associated with lower-amplitude reflections, but also here there are exceptions. For the shear zone shown in Figure 7a, the main contrast at the base of the eclogite layer (at ~500 m) is present in both types of models, meaning peak amplitudes of the models with sharp and smooth transitions differ by less than ~30% at 20 Hz. For the 5 Hz wavelet, the peak reflection is even larger for the smooth compared to that for the sharp transition model, presumably because the reflection from the contrast near the base of the model (at ~100 m) is sufficiently well separated in time to not interfere constructively with the main reflection, while in the smooth transition model this second contrast is felt over a larger depth range. For the shear zones in Figures 7b and 7c the peak amplitudes and total energy reflected is reduced significantly at 20 Hz, but the peak amplitude in the smooth model still is 30–50% of its amplitude in the sharp model, meaning that the shear zones would be harder to see in a real survey but certainly also not become invisible. For these two shear zone models, at 5 Hz the differences between the smooth and sharp transition models are quite subtle. It is clear that these simple 1D reflection responses cannot readily be applied to the interpretation of seismic field data, but they nevertheless give an impression of the effects of the transition types and the variety of responses from shear zones.

Additionally, we calculated the receiver function response that these shear zones would produce at two different wavelengths (Figure 8) using again the reflectivity method in an implementation for an incipient *P* wave at a single slowness (e.g., Wilde-Piorko et al., 2005) for a slowness of 6.5 s/°. The longer wavelength corresponds to high-resolution teleseismic studies, while the shorter wavelength would only be encountered in receiver functions of deep local earthquakes. As these receiver function responses isolate the shear zones rather than a realistic full crustal stack, they should not be read as realistic seismograms.

The amplitude of the conversions is quite small because the material contrasts between the end-member lithologies represented in Figure 7 is not that large. The multiples show more details than do the direct conversions because a given vertical distance maps into a larger time separation. Although the multiples require more lateral heterogeneity to be easily interpretable, the better resolving power of multiples can frequently be found in actual seismograms. A surprising observation is that the (more realistic) smooth shear zone model of Figure 7a results in higher amplitudes than does the corresponding model with sharp transitions.

The variation of seismic anisotropies, however, would probably vary in a different way to the isotropic transitions just discussed. Although the strength of the anisotropy is also expected to decrease from the shear zone center outward, this decrease is likely to be less pronounced because the eclogite breccia around shear zones is also strongly sheared. Additionally, the preserved granulite blocks are elongated parallel to the eclogite foliation, potentially also influencing the magnitude of anisotropy. For these reasons we would expect anisotropy to retain a sharper contrast at the border from eclogite breccia to unaltered granulite at
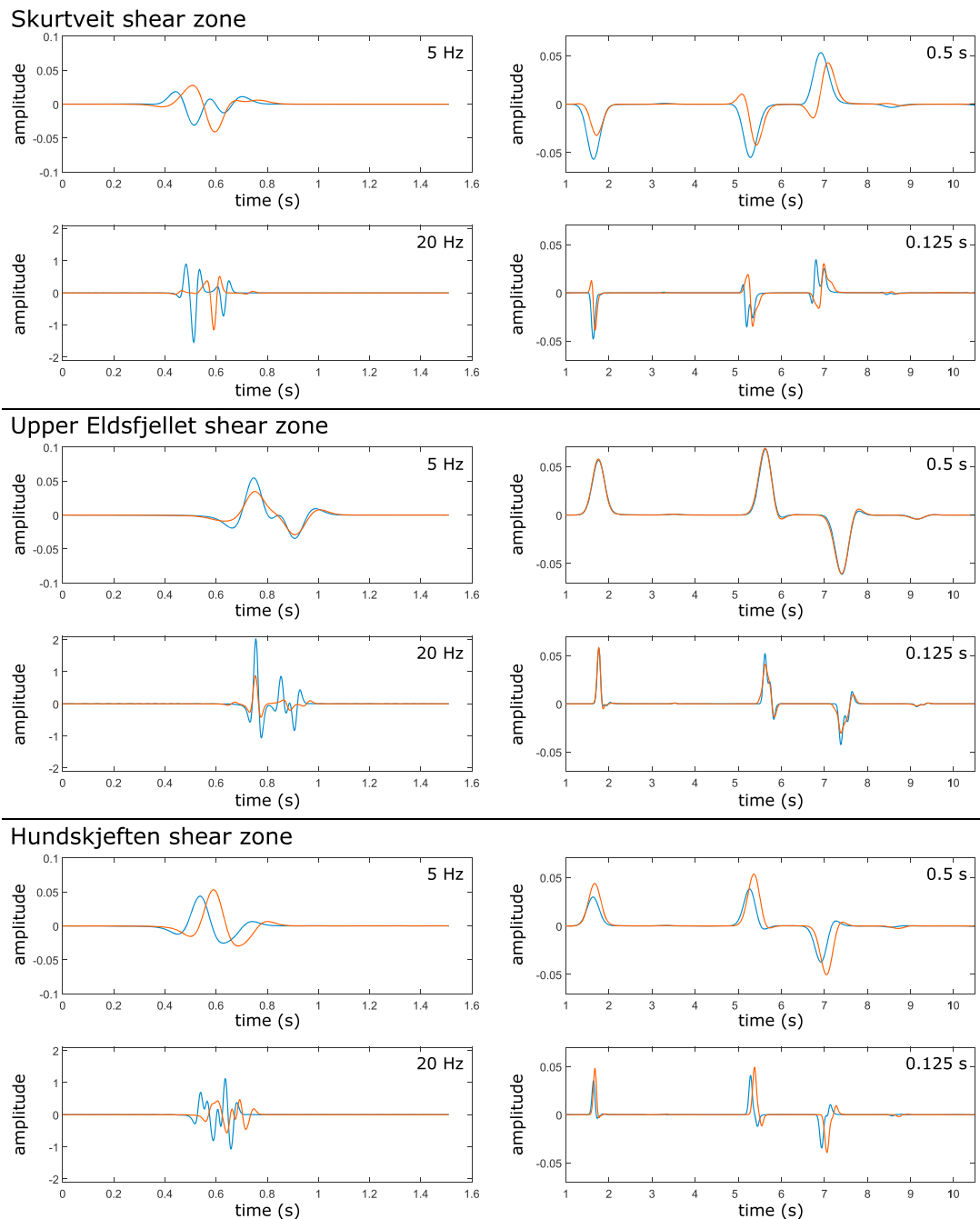
Figure 8. *P* wave (left) reflection response and (right) receiver function response of the shear zones shown in Figure 7. Blue lines refer to the models from Figure 7 with sharp boundaries and constant velocities throughout each layer. Orange lines refer to the models with smooth boundaries and varying velocities throughout each layer. *P* wave reflection responses are shown for 5 and 20 Hz. For receiver function responses the nominal frequency is given as the inverse of the pulse length of the Gaussian-shaped impulse, corresponding approximately to the highest frequency present. For the upper one of each seismogram pair, the pulse length is about 0.5 s, which is the highest, which might realistically be achieved with teleseismic studies. The lower seismograms have a pulse length of 0.125 s, which could apply to local receiver function studies, utilizing for example deep local earthquakes. Note that the first major pulse corresponds to the direct conversion (*Ps* phase), the second pulse to the first multiple (*Ppps*), and the third pulse to the second multiple (*PpSs* + *PsPs*). The absolute times of the arrival of the direct wave and the multiples are of no significance, as the depth of the shear zones has simply been set to be able to conveniently plot the direct wave and its multiples in the same seismogram at sufficiently large scale.

least for some propagation directions. Furthermore, our results suggest that not only seismic velocities vary in different directions through the rock but that this anisotropy also results in a directional dependence of V_P/V_S ratios. This means that specifically receiver function studies, which are sensitive to variations in

V_P/V_S ratios, could be strongly influenced by such structures. In particular, as the earthquake distribution is usually strongly azimuthally biased, an unrepresentative V_P/V_S ratio may be inferred due to anisotropy. A dependence of the backazimuth of the sampled rays on the retrieved receiver function signal was, for example, demonstrated by Nabelek et al. (2009) for the Indian lower crust beneath the Himalaya. Additionally, the results of receiver function analysis are frequently interpreted with petrological modeling software without taking anisotropy into account. For example, Schiffer et al. (2016) imaged a complex structure below East Greenland, interpreted to be a fossil subduction complex. A strongly mafic composition was inferred for a dipping crustal slab, primarily based on high V_P/V_S ratios, but as most of the events underpinning this finding have northern backazimuths, it is also possible that the structure has been sampled along the fast direction and the composition is actually not as extreme.

Although active and passive seismological studies of subduction/collision systems can only provide a snapshot of ongoing processes, it stands to reason that different stages of the eclogitization process are observable at different depths within the same system. This poses the question how the eclogitization and deformation processes evolve through time. It is acknowledged that the shear zone systems discussed here evolve from small-scale shear zones and widen with time ultimately combining into shear zone networks (Austrheim, 1987; Jolivet et al., 2005). The shear zones presented in Figure 7 could be qualitatively interpreted to represent different stages through time. The Upper Eldsfjellet shear zone (Figure 7a) is fairly distinct with a limited thickness. The Skurtveit shear zone (Figure 7b), on the other hand, is significantly thicker, considering both the eclogite shear zone itself and the thickness of the adjacent eclogite breccia. The third stage of the evolution is then represented by the Hundskjeften shear zone (Figure 7c), which essentially represents a shear zone network. The calculated reflection coefficients (Figure 7), which are in the range of typical reflection coefficients of crystalline rocks (Hurich & Smithson, 1987), suggest that this inferred temporal evolution leads to a significant weakening of the expected impedance contrast. There are still significant and not too densely spaced impedance contrasts present within the Upper Eldsfjellet shear zone. What is left of these contrasts in the Hundskjeften shear zone, however, is very densely spaced, and reflection coefficients are very small. The three shear zones shown here demonstrate the evolution of the eclogitization process during ongoing ductile deformation, which is accompanied by weakening of the expected reflected or converted seismic phases. This effect will therefore most likely cause the blurring and subsequent disappearance of the seismic signal in the same way the signal of the Indian lower crust fades below the Himalaya-Tibet collision system (e.g., Hetényi et al., 2007).

This cannot be readily transferred to the reflection and receiver function response presented in Figure 8. Ultimately, stuctural associations such as the ones we describe are limited to sizes smaller than those detectable at great depths by both active seismic reflection methods and teleseismic methods. Our results, however, provide an impression of how the seismic response varies with different shear zone geometries. At depth these shear zones will act as an effective medium, and the variations observed from the hand-specimen scale up to the scale of shear zones a few hundred meters thick will interfere and possibly diminish in magnitude. Nevertheless, the distinct variation of seismic velocities, V_P/V_S ratios, and seismic anisotropy can be used as characteristic signatures in seismological studies. Therefore, our results suggest that if the scale of the structural framework is large enough to be resolved by the wavelengths used for seismic imaging, such structures should be imageable at depth. Anisotropy of the shear zone system can also potentially be imaged if there is a good backazimuthal distribution of the seismic sources (Kaviani & Rümpker, 2015; Schulte-Pelkum et al., 2005). Further, our results confirm that the blurring of the receiver function signal typically observed in such studies (e.g., Schneider et al., 2013) could be caused by partial eclogitization via structures similar to those observed on Holsnøy (shear zones and low-strain domains), but possibly at larger scale.

7. Conclusions

In order to interpret the results from large-scale seismological methods, it is imperative to have knowledge of how metamorphism and deformation alter the seismic properties of rocks deeply buried during subduction and collision. Combining calculations of seismic velocities from thermodynamic modeling with laboratory measurements from a slice of lower continental crust overprinted by eclogite-facies shear zones suggests that eclogitization and associated deformation modify the seismic properties in three ways: (1) Eclogitization causes an increase of P and S wave velocities of ~0.8 and ~0.6 km/s, respectively. (2) Eclogitization, when

associated with ductile shear zone formation, causes an increase of the seismic anisotropy (up to 9%), the magnitude of which is linked to the dominant eclogitization mechanism. (3) Eclogite-facies metamorphism of crustal rocks causes a decrease of the V_P/V_S ratio by about 0.04, mostly due to the breakdown of plagioclase.

With regard to large-scale seismic imaging, the structures exposed on Holsnøy are too small to be detected at depth. However, the apparent scale independence of these structures suggests that it is likely that they exist on a larger scale, in active subduction zones. Based on the characteristically varying seismic properties, we conclude that such structures should be detectable using geophysical imaging techniques, particularly using the variation of seismic anisotropy and V_P/V_S ratio that is produced by the granulite-to-eclogite transition. Our results also show conclusively that progressive eclogitization and deformation lead to a decrease of the seismic signal (e.g., receiver function signal) and subsequently erase it entirely with time.

References

Ábalos, B., Fountain, D. M., Gil Ibarguchi, J. I., & Puelles, P. (2011). Eclogite as a seismic marker in subduction channels: Seismic velocities, anisotropy, and petrofabric of Cabo Ortegal eclogite tectonites (Spain). *GSA Bulletin*, *123*(3-4), 439–456. https://doi.org/10.1130/B30226.1

Almqvist, B. S. G., Burg, J. P., Berger, J., & Burlini, L. (2013). Seismic properties of the Kohistan oceanic arc root: Insights from laboratory measurements and thermodynamic modeling. *Geochemistry, Geophysics, Geosystems*, *14*, 1819–1841. https://doi.org/10.1002/ggge.20125

Almqvist, B. S. G., & Mainprice, D. (2017). Seismic properties and anisotropy of the continental crust: Predictions based on mineral texture and rock microstructure. *Reviews of Geophysics*, *55*, 367–433. https://doi.org/10.1002/2016RG000552

Altenberger, U., & Wilhelm, S. (2000). Ductile deformation of K-feldspar in dry eclogite facies shear zones in the Bergen Arcs, Norway. *Tectonophysics*, *320*(2), 107–121. https://doi.org/10.1016/S0040-1951(00)00048-2

Andersen, T. B., Corfu, F., Labrousse, L., & Osmundsen, P.-T. (2012). Evidence for hyperextension along the pre-Caledonian margin of Baltica. *Journal of the Geological Society*, *169*(5), 601–612. https://doi.org/10.1144/0016-76492012-011

Andersen, T. B., Jamtveit, B., Dewey, J. F., & Swensson, E. (1991). Subduction and eduction of continental crust: Major mechanisms during continent-continent collision and orogenic extensional collapse, a model based on the south Norwegian Caledonides. *Terra Nova*, *3*(3), 303–310. https://doi.org/10.1111/j.1365-3121.1991.tb00148.x

Austrheim, H. (1987). Eclogitization of lower crustal granulites by fluid migration through shear zones. *Earth and Planetary Science Letters*, *81*(2-3), 221–232. https://doi.org/10.1016/0012-821X(87)90158-0

Austrheim, H. (1990). The granulite-eclogite facies transition: A comparison of experimental work and a natural occurrence in the Bergen Arcs, western Norway. *Lithos*, *25*(1-3), 163–169. https://doi.org/10.1016/0024-4937(90)90012-P

Austrheim, H., & Boundy, T. M. (1994). Pseudotachylytes generated during seismic faulting and eclogitization of the deep crust. *Science*, *265*(5168), 82–83. https://doi.org/10.1126/science.265.5168.82

Austrheim, H., Dunkel, K. G., Plümper, O., Ildefonse, B., Liu, Y., & Jamtveit, B. (2017). Fragmentation of wall rock garnets during deep crustal earthquakes. *Science Advances*, *3*(2), e1602067. https://doi.org/10.1126/sciadv.1602067

Austrheim, H., & Griffin, W. L. (1985). Shear deformation and eclogite formation within granulite-facies anorthosites of the Bergen Arcs, western Norway. *Chemical Geology*, *50*(1-3), 267–281. https://doi.org/10.1016/0009-2541(85)90124-X

Babuška, V., Fiala, J., Mayson, D. J., & Liebermann, R. C. (1978). Elastic properties of eclogite rocks from the Bohemian Massif. *Studia Geophysica et Geodaetica*, *22*(4), 348–361. https://doi.org/10.1007/BF02179277

Barruol, G., & Kern, H. (1996). Seismic anisotropy and shear-wave splitting in lower-crustal and upper-mantle rocks from the Ivrea Zone—Experimental and calculated data. *Physics of the Earth and Planetary Interiors*, *95*(3-4), 175–194. https://doi.org/10.1016/0031-9201(95)03124-3

Bascou, J., Barruol, G., Vauchez, A., Mainprice, D., & Egydio-Silva, M. (2001). EBSD-measured lattice-preferred orientations and seismic properties of eclogites. *Tectonophysics*, *342*(1-2), 61–80. https://doi.org/10.1016/S0040-1951(01)00156-1

Bhowany, K., Hand, M., Clark, C., Kelsey, D. E., Reddy, S. M., Pearce, M. A., et al. (2017). Phase equilibria modelling constraints on *P–T* conditions during fluid catalysed conversion of granulite to eclogite in the Bergen Arcs, Norway. *Journal of Metamorphic Geology*, *36*(3), 315–342. https://doi.org/10.1111/jmg.12294

Bingen, B., Austrheim, H., & Whitehouse, M. (2001). Ilmenite as a source for zirconium during high-grade metamorphism? Textural evidence from the Caledonides of western Norway and implications for zircon geochronology. *Journal of Petrology*, *42*(2), 355–375. https://doi.org/10.1093/petrology/42.2.355

Bloch, W., John, T., Kummerow, J., Salazar, P., Krüger, O. S., & Shapiro, S. A. (2018). Watching dehydration: Seismic indication for transient fluid pathways in the oceanic mantle of the subducting Nazca slab. *Geochemistry, Geophysics, Geosystems*, *19*, 3189–3207. https://doi.org/10.1029/2018GC007703

Bostock, M., Hyndman, R., Rondenay, S., & Peacock, S. (2002). An inverted continental Moho and serpentinization of the forearc mantle. *Nature*, *417*(6888), 536–538. https://doi.org/10.1038/417536a

Boundy, T. M., Fountain, D. M., & Austrheim, H. (1992). Structural development and petrofabrics of eclogite facies shear zones, Bergen Arcs, western Norway: Implications for deep crustal deformational processes. *Journal of Metamorphic Geology*, *10*(2), 127–146. https://doi.org/10.1111/j.1525-1314.1992.tb00075.x

Brown, D., Llana-Funez, S., Carbonell, R., Alvarez-Marron, J., Marti, D., & Salisbury, M. (2009). Laboratory measurements of P-wave and S-wave velocities across a surface analog of the continental crust-mantle boundary: Cabo Ortegal, Spain. *Earth and Planetary Science Letters*, *285*(1-2), 27–38. https://doi.org/10.1016/j.epsl.2009.05.032

Brown, J. M., Abramson, E. H., & Angel, R. J. (2006). Triclinic elastic constants for low albite. *Physics and Chemistry of Minerals*, *33*(4), 256–265. https://doi.org/10.1007/s00269-006-0074-1

Brown, J. M., Angel, R. J., & Ross, N. L. (2016). Elasticity of plagioclase feldspars. *Journal of Geophysical Research: Solid Earth*, *121*, 663–675. https://doi.org/10.1002/2015JB012736

Christensen, N. I. (1996). Poisson's ratio and crustal seismology. *Journal of Geophysical Research*, *101*(B2), 3139–3156. https://doi.org/10.1029/95JB03446

Connolly, J. A. D. (2005). Computation of phase equilibria by linear programming: A tool for geodynamic modeling and its application to subduction zone decarbonation. *Earth and Planetary Science Letters*, *236*(1-2), 524–541. https://doi.org/10.1016/j.epsl.2005.04.033

Connolly, J. A. D., & Kerrick, D. M. (2002). Metamorphic controls on seismic velocity of subducted oceanic crust at 100–250 km depth. *Earth and Planetary Science Letters*, *204*(1-2), 61–74. https://doi.org/10.1016/S0012-821X(02)00957-3

Corfu, F., Andersen, T. B., & Gasser, D. (2014). The Scandinavian Caledonides: Main features, conceptual advances and critical questions. *Geological Society, London, Special Publications*, *390*(1), 9–43. https://doi.org/10.1144/sp390.25

Diener, J. F. A., Powell, R., White, R. W., & Holland, T. J. B. (2007). A new thermodynamic model for clino- and orthoamphiboles in the system Na$_2$O–CaO–FeO–MgO–Al$_2$O$_3$–SiO$_2$–H$_2$O–O. *Journal of Metamorphic Geology*, *25*(6), 631–656. https://doi.org/10.1111/j.1525-1314.2007.00720.x

Dreiling, J., Tilmann, F., Yuan, X., Giese, J., Rindraharisaona, E. J., Rümpker, G., & Wysession, M. E. (2018). Crustal radial anisotropy and linkage to geodynamic processes: A study based on seismic ambient noise in southern Madagascar. *Journal of Geophysical Research: Solid Earth*, *123*, 5130–5146. https://doi.org/10.1029/2017JB015273

Faccenda, M., Ferreira, A. M. G., Tisato, N., Lithgow-Bertelloni, C., Stixrude, L., & Pennacchioni, G. (2019). Extrinsic elastic anisotropy in a compositionally heterogeneous Earth's mantle. *Journal of Geophysical Research: Solid Earth*, *124*, 1671–1687. https://doi.org/10.1029/2018JB016482

Fountain, D. M., Boundy, T. M., Austrheim, H., & Rey, P. (1994). Eclogite-facies shear zones—Deep crustal reflectors? *Tectonophysics*, *232*(1-4), 411–424. https://doi.org/10.1016/0040-1951(94)90100-7

Fowler, C. M. R. (2005). *The solid Earth: An introduction to global geophysics*. New York, NY: Cambridge University Press.

Fuchs, K., & Müller, G. (1971). Computation of synthetic seismogram with reflectivity method and comparison with observations. *Geophysical Journal of the Royal Astronomical Society*, *23*(4), 417–433. https://doi.org/10.1111/j.1365-246X.1971.tb01834.x

Furman, M. L., & Lindsley, D. H. (1988). Ternary-feldspar modeling and thermometry. *American Mineralogist*, *73*(3-4), 201–215.

Glodny, J., Kühn, A., & Austrheim, H. (2008). Geochronology of fluid-induced eclogite and amphibolite facies metamorphic reactions in a subduction–collision system, Bergen Arcs, Norway. *Contributions to Mineralogy and Petrology*, *156*(1), 27–48. https://doi.org/10.1007/s00410-007-0272-y

Green, E., Holland, T., & Powell, R. (2007). An order-disorder model for omphacitic pyroxenes in the system jadeite-diopside-hedenbergite-acmite, with applications to eclogitic rocks. *American Mineralogist*, *92*(7), 1181–1189. https://doi.org/10.2138/am.2007.2401

Hacker, B. R., Abers, G. A., & Peacock, S. M. (2003). Subduction factory 1. Theoretical mineralogy, densities, seismic wave speeds, and H$_2$O contents. *Journal of Geophysical Research*, *108*(B1), 2029. https://doi.org/10.1029/2001JB001127

Halpaap, F., Rondenay, S., & Ottemöller, L. (2018). Seismicity, deformation, and metamorphism in the Western Hellenic Subduction Zone: New constraints from tomography. *Journal of Geophysical Research: Solid Earth*, *123*, 3000–3026. https://doi.org/10.1002/2017JB015154

Hawemann, F., Mancktelow, N. S., Pennacchioni, G., Wex, S., & Camacho, A. (2019). Weak and slow, strong and fast: How shear zones evolve in a dry continental crust (Musgrave Ranges, Central Australia). *Journal of Geophysical Research: Solid Earth*, *124*, 219–240. https://doi.org/10.1029/2018JB016559

Hetényi, G., Cattin, R., Brunet, F., Bollinger, L., Vergne, J., Nábělek, J. L., & Diament, M. (2007). Density distribution of the India plate beneath the Tibetan Plateau: Geophysical and petrological constraints on the kinetics of lower-crustal eclogitization. *Earth and Planetary Science Letters*, *264*(1-2), 226–244. https://doi.org/10.1016/j.epsl.2007.09.036

Hill, R. (1952). The elastic behaviour of a crystalline aggregate. *Proceedings of the Physical Society. Section A*, *65*(5), 349–354. https://doi.org/10.1088/0370-1298/65/5/307

Holland, T., & Powell, R. (1996). Thermodynamics of order-disorder in minerals: II. Symmetric formalism applied to solid solutions. *American Mineralogist*, *81*(11-12), 1425–1437. https://doi.org/10.2138/am-1996-11-1215

Holland, T. J. B., & Powell, R. (1998). An internally consistent thermodynamic data set for phases of petrological interest. *Journal of Metamorphic Geology*, *16*(3), 309–343. https://doi.org/10.1111/j.1525-1314.1998.00140.x

Hurich, C. A., & Smithson, S. B. (1987). Compositional variation and the origin of deep crustal reflections. *Earth and Planetary Science Letters*, *85*(4), 416–426. https://doi.org/10.1016/0012-821X(87)90137-3

Incel, S., Labrousse, L., Hilairet, N., John, T., Gasc, J., Shi, F., et al. (2019). Reaction-induced embrittlement of the lower continental crust. *Geology*, *47*(3), 235–238. https://doi.org/10.1130/G45527.1

Jackson, J. A., Austrheim, H., McKenzie, D., & Priestley, K. (2004). Metastability, mechanical strength, and the support of mountain belts. *Geology*, *32*(7), 625–628. https://doi.org/10.1130/G20397.1

Jakob, J., Alsaif, M., Corfu, F., & Andersen, T. B. (2017). Age and origin of thin discontinuous gneiss sheets in the distal domain of the magma-poor hyperextended pre-Caledonian margin of Baltica, southern Norway. *Journal of the Geological Society*, *174*(3), 557–571. https://doi.org/10.1144/jgs2016-049

Jakob, J., Andersen, T. B., & Kjøll, H. J. (2019). A review and reinterpretation of the architecture of the South and South-Central Scandinavian Caledonides—A magma-poor to magma-rich transition and the significance of the reactivation of rift inherited structures. *Earth-Science Reviews*, *192*, 513–528. https://doi.org/10.1016/j.earscirev.2019.01.004

Jamtveit, B., Austrheim, H., & Malthe-Sorenssen, A. (2000). Accelerated hydration of the Earth's deep crust induced by stress perturbations. *Nature*, *408*(6808), 75–78. https://doi.org/10.1038/35040537

Jamtveit, B., Ben-Zion, Y., Renard, F., & Austrheim, H. (2018). Earthquake-induced transformation of the lower crust. *Nature*, *556*(7702), 487–491. https://doi.org/10.1038/s41586-018-0045-y

Jamtveit, B., Bucher-Nurminen, K., & Austrheim, H. (1990). Fluid controlled eclogitization of granulites in deep crustal shear zones, Bergen arcs, western Norway. *Contributions to Mineralogy and Petrology*, *104*(2), 184–193. https://doi.org/10.1007/bf00306442

John, T., & Schenk, V. (2003). Partial eclogitisation of gabbroic rocks in a late Precambrian subduction zone (Zambia): Prograde metamorphism triggered by fluid infiltration. *Contributions to Mineralogy and Petrology*, *146*(2), 174–191. https://doi.org/10.1007/s00410-003-0492-8

Jolivet, L., Raimbourg, H., Labrousse, L., Avigad, D., Leroy, Y., Austrheim, H., & Andersen, T. B. (2005). Softening trigerred by eclogitization, the first step toward exhumation during continental subduction. *Earth and Planetary Science Letters*, *237*(3–4), 532–547. https://doi.org/10.1016/j.epsl.2005.06.047

Kaviani, A., & Rümpker, G. (2015). Generalization of the *H-κ* stacking method to anisotropic media. *Journal of Geophysical Research: Solid Earth*, *120*, 5135–5153. http://doi.org/10.1002/2014JB011858

Keppler, R., Behrmann, J. H., & Stipp, M. (2017). Textures of eclogites and blueschists from Syros island, Greece: Inferences for elastic anisotropy of subducted oceanic crust. *Journal of Geophysical Research: Solid Earth*, *122*, 5306–5324. https://doi.org/10.1002/2017JB014181

Keppler, R., Ullemeyer, K., Behrmann, J. H., & Stipp, M. (2014). Potential of full pattern fit methods for the texture analysis of geological materials: Implications from texture measurements at the recently upgraded neutron time-of-flight diffractometer SKAT. *Journal of Applied Crystallography*, *47*(5), 1520–1534. https://doi.org/10.1107/S1600576714015830

Kern, H. (1978). The effect of high temperature and high confining pressure on compressional wave velocities in quartz-bearing and quartz-free igneous and metamorphic rocks. *Tectonophysics*, *44*(1-4), 185–203. https://doi.org/10.1016/0040-1951(78)90070-7

Kern, H., & Fakhimi, M. (1975). Effect of fabric anisotropy on compressional-wave propagation in various metamorphic rocks for the range 20–700°C at 2 kbars. *Tectonophysics*, *28*(4), 227–244. https://doi.org/10.1016/0040-1951(75)90039-6

Kern, H., Gao, S., Jin, Z., Popp, T., & Jin, S. (1999). Petrophysical studies on rocks from the Dabie ultrahigh-pressure (UHP) metamorphic belt, Central China: Implications for the composition and delamination of the lower crust. *Tectonophysics*, *301*(3-4), 191–215. https://doi.org/10.1016/S0040-1951(98)00268-6

Kern, H., Gao, S., & Liu, Q.-S. (1996). Seismic properties and densities of middle and lower crustal rocks exposed along the North China Geoscience Transect. *Earth and Planetary Science Letters*, *139*(3-4), 439–455. https://doi.org/10.1016/0012-821X(95)00240-D

Kern, H., Liu, B., & Popp, T. (1997). Relationship between anisotropy of *P* and *S* wave velocities and anisotropy of attenuation in serpentinite and amphibolite. *Journal of Geophysical Research*, *102*(B2), 3051–3065. https://doi.org/10.1029/96jb03392

Kind, R., Yuan, X., & Kumar, P. (2012). Seismic receiver functions and the lithosphere–asthenosphere boundary. *Tectonophysics*, *536-537*, 25–43. https://doi.org/10.1016/j.tecto.2012.03.005

Labrousse, L., Hetényi, G., Raimbourg, H., Jolivet, L., & Andersen, T. B. (2010). Initiation of crustal-scale thrusts triggered by metamorphic reactions at depth: Insights from a comparison between the Himalayas and Scandinavian Caledonides. *Tectonics*, *29*, TC5002. https://doi.org/10.1029/2009TC002602

Lloyd, G. E., Butler, R. W. H., Casey, M., Tatham, D. J., & Mainprice, D. (2011). Constraints on the seismic properties of the middle and lower continental crust. *Geological Society, London, Special Publications*, *360*(1), 7–32. https://doi.org/10.1144/sp360.2

Lloyd, G. E., Halliday, J. M., Butler, R. W. H., Casey, M., Kendall, J.-M., Wookey, J., & Mainprice, D. (2011). From crystal to crustal: Petrofabric-derived seismic modelling of regional tectonics. *Geological Society, London, Special Publications*, *360*(1), 49–78. https://doi.org/10.1144/sp360.4

Lutterotti, L., Matthies, S., Wenk, H.-R., Schultz, A. S., & Richardson, J. W. (1997). Combined texture and structure analysis of deformed limestone from time-of-flight neutron diffraction spectra. *Journal of Applied Physics*, *81*(2), 594–600. https://doi.org/10.1063/1.364220

Manghnani, M. H., Ramananantoandro, R., & Clark, S. P. (1974). Compressional and shear wave velocities in granulite facies rocks and eclogites to 10 kbar. *Journal of Geophysical Research*, *79*(35), 5427–5446. https://doi.org/10.1029/JB079i035p05427

Mauler, A., Burlini, L., Kunze, K., Philippot, P., & Burg, J.-P. (2000). P-wave anisotropy in eclogites and relationship to the omphacite crystallographic fabric. *Physics and Chemistry of the Earth, Part A: Solid Earth and Geodesy*, *25*(2), 119–126. https://doi.org/10.1016/S1464-1895(00)00020-X

Menegon, L., Pennacchioni, G., Malaspina, N., Harris, K., & Wood, E. (2017). Earthquakes as precursors of ductile shear zones in the dry and strong lower crust. *Geochemistry, Geophysics, Geosystems*, *18*, 4356–4374. https://doi.org/10.1002/2017GC007189

Mooney, W. D., & Meissner, R. (1992). Multi-genetic origin of crustal reflectivity: A review of seismic reflection profiling of the continental lower crust and Moho. In D. M. Fountain, R. Arculus, & R. W. Kay (Eds.), *Continental lower crust* (pp. 45–79). Amsterdam: Elsevier.

Motra, H. B., & Zertani, S. (2018). Influence of loading and heating processes on elastic and geomechanical properties of eclogites and granulites. *Journal of Rock Mechanics and Geotechnical Engineering*, *10*(1), 127–137. https://doi.org/10.1016/j.jrmge.2017.11.001

Nabelek, J., Hetenyi, G., Vergne, J., Sapkota, S., Kafle, B., Jiang, M., et al. (2009). Underplating in the Himalaya-Tibet collision zone revealed by the Hi-CLIMB experiment. *Science*, *325*(5946), 1371–1374. https://doi.org/10.1126/science.1167719

Olive, J.-A., Pearce, F., Rondenay, S., & Behn, M. D. (2014). Pronounced zonation of seismic anisotropy in the Western Hellenic subduction zone and its geodynamic significance. *Earth and Planetary Science Letters*, *391*, 100–109. https://doi.org/10.1016/j.epsl.2014.01.029

Petley-Ragan, A., Dunkel, K. G., Austrheim, H., Ildefonse, B., & Jamtveit, B. (2018). Microstructural records of earthquakes in the lower crust and associated fluid-driven metamorphism in plagioclase-rich granulites. *Journal of Geophysical Research: Solid Earth*, *123*, 3729–3746. https://doi.org/10.1029/2017JB015348

Raimbourg, H., Jolivet, L., Labrousse, L., Leroy, Y., & Avigad, D. (2005). Kinematics of syneclogite deformation in the Bergen Arcs, Norway: Implications for exhumation mechanisms. *Geological Society, London, Special Publications*, *243*(1), 175–192. https://doi.org/10.1144/gsl.sp.2005.243.01.13

Rey, P. F., Fountain, D. M., & Clement, W. P. (1994). P wave velocity across a noncoaxial ductile shear zone and its associated strain gradient: Consequences for upper crustal reflectivity. *Journal of Geophysical Research*, *99*(B3), 4533–4548. https://doi.org/10.1029/93JB03105

Rondenay, S., Abers, G. A., & van Keken, P. E. (2008). Seismic imaging of subduction zone metamorphism. *Geology*, *36*(4), 275–278. https://doi.org/10.1130/G24112A.1

Rondenay, S., Bostock, M., & Shragge, J. (2001). Multiparameter two-dimensional inversion of scattered teleseismic body waves 3. Application to the Cascadia 1993 data set. *Journal of Geophysical Research*, *106*(B12), 30,795–30,807. https://doi.org/10.1029/2000JB000039

Rondenay, S., Bostock, M. G., & Fischer, K. M. (2005). Multichannel inversion of scattered teleseismic body waves: Practical considerations and applicability. In A. Levander, & G. Nolet (Eds.), *Seismic Earth: Array analysis of broadband seismograms*, *AGU Geophysical Monograph Series* (Vol. 157, pp. 187–203). Wiley. https://doi.org/10.1029/157GM12

Sandmeier, K.-J., & Wenzel, F. (1986). Synthetic seismograms for a complex crustal model. *Geophysical Research Letters*, *13*(1), 22–25. https://doi.org/10.1029/GL013i001p00022

Scambelluri, M., Pennacchioni, G., Gilio, M., Bestmann, M., Plümper, O., & Nestola, F. (2017). Fossil intermediate-depth earthquakes in subducting slabs linked to differential stress release. *Nature Geoscience*, *10*(12), 960–966. https://doi.org/10.1038/s41561-017-0010-7

Schiffer, C., Balling, N., Ebbing, J., Jacobsen, B. H., & Nielsen, S. B. (2016). Geophysical-petrological modelling of the East Greenland Caledonides—Isostatic support from crust and upper mantle. *Tectonophysics*, *692*, 44–57. https://doi.org/10.1016/j.tecto.2016.06.023

Schiffer, C., Jacobsen, B. H., Balling, N., Ebbing, J., & Nielsen, S. B. (2015). The East Greenland Caledonides—Teleseismic signature, gravity and isostasy. *Geophysical Journal International*, *203*(2), 1400–1418. https://doi.org/10.1093/gji/ggv373

Schneider, F. M., Yuan, X., Schurr, B., Mechie, J., Sippl, C., Haberland, C., et al. (2013). Seismic imaging of subducting continental lower crust beneath the Pamir. *Earth and Planetary Science Letters*, *375*, 101–112. https://doi.org/10.1016/j.epsl.2013.05.015

Schulte-Pelkum, V., Monsalve, G., Sheehan, A., Pandey, M. R., Sapkota, S., Bilham, R., & Wu, F. (2005). Imaging the Indian subcontinent beneath the Himalaya. *Nature*, *435*(7046), 1222–1225. https://doi.org/10.1038/nature03678

Ullemeyer, K., Spalthoff, P., Heinitz, J., Isakov, N. N., Nikitin, A. N., & Weber, K. (1998). The SKAT texture diffractometer at the pulsed reactor IBR-2 at Dubna: experimental layout and first measurements. *Nuclear Instruments and Methods in Physics Research Section A: Accelerators, Spectrometers, Detectors and Associated Equipment*, *412*(1), 80–88. https://doi.org/10.1016/S0168-9002(98)00340-4

Wang, Q., Shaocheng, J., Salisbury, M. H., Xia, B., Pan, M., & Xu, Z. (2005a). Pressure dependence and anisotropy of P-wave velocities in ultrahigh-pressure metamorphic rocks from the Dabie-Sulu orogenic belt (China): Implications for seismic properties of subducted slabs and origin of mantle reflections. *Tectonophysics*, *398*(1-2), 67–99. https://doi.org/10.1016/j.tecto.2004.12.001

Wang, Q., Shaocheng, J., Salisbury, M. H., Xia, B., Pan, M., & Xu, Z. (2005b). Shear wave properties and Poisson's ratios of ultrahigh-pressure metamorphic rocks from the Dabie-Sulu orogenic belt, China: Implications for crustal composition. *Journal of Geophysical Research*, *110*, B08208. https://doi.org/10.1029/2004JB003435

Weiss, T., Siegesmund, S., Rabbel, W., Bohlen, T., & Pohl, M. (1999). Seismic velocities and anisotropy of the lower continental crust: A review. In D. Gajewski, & W. Rabbel (Eds.), *Seismic exploration of the deep continental crust: Methods and concepts of DEKORP and accompanying projects*, *Pure and Applied Geophysics* (pp. 97–122). Basel: Birkhäuser Verlag. https://doi.org/10.1007/978-3-0348-8670-3_6

White, R. W., Pomroy, N. E., & Powell, R. (2005). An in situ metatexite–diatexite transition in upper amphibolite facies rocks from Broken Hill, Australia. *Journal of Metamorphic Geology*, *23*(7), 579–602. https://doi.org/10.1111/j.1525-1314.2005.00597.x

Wilde-Piorko, M., Saul, J., & Grad, M. (2005). Differences in the crustal and uppermost mantle structure of the Bohemian Massif from teleseismic receiver functions. *Studia Geophysica et Geodetica*, *49*(1), 85–107. https://doi.org/10.1007/s11200-005-1627-3

Worthington, J. R., Hacker, B. R., & Zandt, G. (2013). Distinguishing eclogite from peridotite: EBSD-based calculations of seismic velocities. *Geophysical Journal International*, *193*(1), 489–505. https://doi.org/10.1093/gji/ggt004

Zertani, S., Labrousse, L., John, T., Andersen, T. B., & Tilmann, F. (2019). The interplay of eclogitization and deformation during deep burial of lower crust—A case study from the Bergen Arcs (western Norway). *Tectonics*, *38*, 898–915. https://doi.org/10.1029/2018TC005297

Zhang, H., Thruber, C. H., Shelly, D., Ide, S., Beroza, G. C., & Hasegawa, A. (2004). High-resolution subducting-slab structure beneath northern Honshu, Japan, revealed by double-difference tomography. *Geology*, *32*(4), 361–364. https://doi.org/10.1130/G20261.2

Zhong, X., Frehner, M., Kunze, K., & Zappone, A. (2014). A novel EBSD-based finite-element wave propagation model for investigating seismic anisotropy: Application to Finero Peridotite, Ivrea-Verbano Zone, Northern Italy. *Geophysical Research Letters*, *41*, 7105–7114. https://doi.org/10.1002/2014GL060490